WATER-DISPERSIBLE $Ti_3C_2T_Z$ MXene NANOSHEETS BY ACID FREE, MOLTEN SALT ETCHING

A Thesis

by

KAILASH DHONDIRAM AROLE

Submitted to the Office of Graduate and Professional Studies of
Texas A&M University
in partial fulfilment of the requirements for the degree of

MASTER OF SCIENCE

Chair of Committee,	Micah Green
Committee Members,	Miladin Radovic
	Emily Pentzer
Head of Department,	Ibrahim Karaman

May 2021

Major Subject: Materials Science and Engineering

ABSTRACT

Current methods to produce 2D $Ti_3C_2T_z$ (MXene) nanosheets require hazardous HF for etching of the Ti_3AlC_2 MAX phase. Here, a molten salt (SnF_2) etching method that produces water dispersible $Ti_3C_2T_z$ nanosheets without the need for HF is introduced. In molten salt etching, SnF_2 may diffused in between the layers during etching to form AlF_3 and Sn as byproducts. Sn spheres form internally in the layers to push the layers apart and form large d-spacings. The stable, aqueous $Ti_3C_2T_z$ nanosheet dispersion yields a ζ potential of -31.7 mV, owing to -OH terminal groups introduced from a KOH wash. X-ray diffraction and electron microscopy confirm the formation of $Ti_3C_2T_z$ etched clay with substantial d-spacing as compared to the clay from a traditional HF-process. This work is the first to use molten salt etching to successfully prepare colloidally stable aqueous dispersions of $Ti_3C_2T_z$ nanosheets. The $Ti_3C_2T_z$ nanosheet film and clay produced by this method also show excellent conductivity, specific and areal capacitance.

DEDICATION

To

Mon and Dad

ACKNOWLEDGEMENTS

Firstly, I would like to express my sincere gratitude to my principal investigator, Dr. Micah Green whose constant inspiration and support was the greatest driving force in the completion of my thesis throughout the entire duration of two years. I couldn't have asked for a better academic thesis advisor; he has always shown me the right direction through his research insights. He has always challenged me to push my limits and find another perspective to look at a problem. He has taught me how to see each problem in a different light and how to investigate the true underlying issue. I have learned many valuable skills during my research with Dr. Green and I am grateful for all that he has done for me as an academic advisor. I am indebted to him for his invaluable guidance which was monumental in my successful submission of a first-authored paper in a journal along with few co-authored papers.

I would also like to thank Dr. Miladin Radovic and Dr. Emily Pentzer from the Department of Materials Science and Engineering at Texas A&M University for taking some precious time out of their busy schedule and agreeing to be a part of my committee. In addition, I am also grateful to Erin Bandza for helping me out with all rules and regulations required at every step of my master's thesis.

I would like to express my appreciation to Xiaofei Zhao for being the mentor and training me on all the required equipment's in our laboratory. I would also like to pay special regards to my research group colleagues Dr. Tezel, Sanjit Saha, Pawan Verma, Anubhav Sarmah, Huaixuan Cao for helping me innumerable times with their research advise. I am also thankful to other members of the group for their constructive feedback during group meetings.

I would like to thank my constant support system, my mom and dad. You are the driving force behind l my thirst for knowledge and intellectual curiosity. You have pushed me through the years to achieve more than I thought was possible. I feel lucky to have found such great friends at Texas A&M University who always supported me in my all ups and downs. They have made my master's journey the best two years of my life and I couldn't have asked for anything better.

CONTRIBUTORS AND FUNDING SOURCE

Contributors

This work was supervised by a thesis committee consisting of my advisor, Dr. Micah Green from Artie McFerrin department of Chemical engineering and my committee members, Dr. Miladin Radovic and Dr. Emily Pentzer from Department of Materials Science and Engineering. The constant support of Dr. Jodie Lutkenhaus from Department of Chemical Engineering at Texas A&M University was really helpful.

Most of my MXene etching was administered by Xiaofei Zhao a Chemical Engineering Ph.D. candidate in Dr. Green's research group. Xiaofei was especially helpful in the initial stages of this study, as I was becoming familiar with the equipment in the Green lab. I would also like to extend thanks to Jackson Bilvin, an undergraduate researcher in Dr. Green's lab. Devon has assisted me during my initial days of research in Dr. Green's lab.

Supercapacitor data was analyzed by Dr. Sanjit Saha, a Chemical Engineering Posy-doctoral candidate in Dr. Green's research group. RF data and Transmission Electron Images were provided by Anubhav Sarmah and Hu and Huaixuan Cao respectively. MAX powders required for the etching was provided by Dustin Holta.

All other work conducted for the thesis was completed by the student independently.

Funding Source:

This work is funded by National Science Foundation (Grant CMMI-1760859).

NOMENCLATURE

KOH Potassium Hydroxide

DMSO Dimethyl Sulfoxide

SEM Scanning Electron Microscope

EDS Energy Dispersive X-ray Spectroscopy

TEM Transmission Electron Microscopy

XRD X-Ray Diffraction

AFM Atomic Force Microscopy

RF Radio Frequency

PVDF Polyvinylidene fluoride

CV Cyclic Voltammetry

C-D Charge-Discharge

TABLE OF CONTENTS

Page

LIST OF FIGURES

Page

LIST OF TABLES

Page

CHAPTER I

INTRODUCTION

MXenes are a class of two-dimensional inorganic materials invented in 2011 by Naguib *et. al*. MXenes have caught the world's attention because of their wide compositional diversity and ability to modify them for many applications[1]. The variety of compositions and structures of MXenes has led to the large and fast-growing family of 2D materials. MXene is a few-atoms-thick layers of transition metal carbides, nitrides, or carbonitrides. MXenes are generally prepared by the selective etching of the A-layer element from a MAX phase parent material[2]. The surface terminations, which are generally –F, –Cl, –OH, or =O bonded to the outer M layers of the MXene. These terminal functional groups contribute towards a wide range of properties such as metallic conductivity and hydrophilicity, which have broad applications in actuators, energy storage, catalysis, electromagnetic interference shielding, sensor, composites, and batteries[3-11].

The method of production of MXene at industry level must be chosen based on cost, safety, and scalability. MXenes have been generally prepared by the selective etching of the A-layer in an aqueous solution containing fluoride ions such as aqueous hydrofluoric acid (HF)[1, 2, 12]. Other methods include utilizing an *in-situ* technique to make HF with a mixture of hydrochloric acid (HCl) and lithium fluoride (LiF) or ammonium bifluoride $(NH_4)HF_2$. The major drawbacks of HF-related methods are the dangers associated with using HF, along with waste management and scalability[13]. Apart from the routes, that use HF, an alternative electrochemical fluoride-free synthesis route is also been reported, for example, in dilute hydrochloric acid, was recently

reported for Ti_2CT_z MXene synthesis[14]. However, scaling up selective electrochemical etching methods at industry level may be a challenging task.

However, challenges with advanced and scalable manufacturing of MXenes still prevent their broad distribution and implementation, including maximizing yield and quality while minimizing the need for hazardous HF etchant. A new method to make MXene has been invented recently called "molten salt etching"[15]. In this method, a mixture of MAX phase powder and molten salt is heated to make MXenes. The only disadvantage of this work so far is the colloidal instability of the aqueous dispersion of MXene nanosheets. This work will experimentally investigate this challenge in support of the long-term goal of accessing high-quality, high-yield MXenes nanosheets aqueous dispersion for advanced applications. We have proposed the KOH wash to the MXene clay before delamination and sonication, which will basically replace some of the halide terminal groups (fluoride in our case) with hydroxyl groups (-OH) providing the colloidal stability to dispersion. **Figure 1** shows the setup used in the synthesis of MXene by molten salt etching.

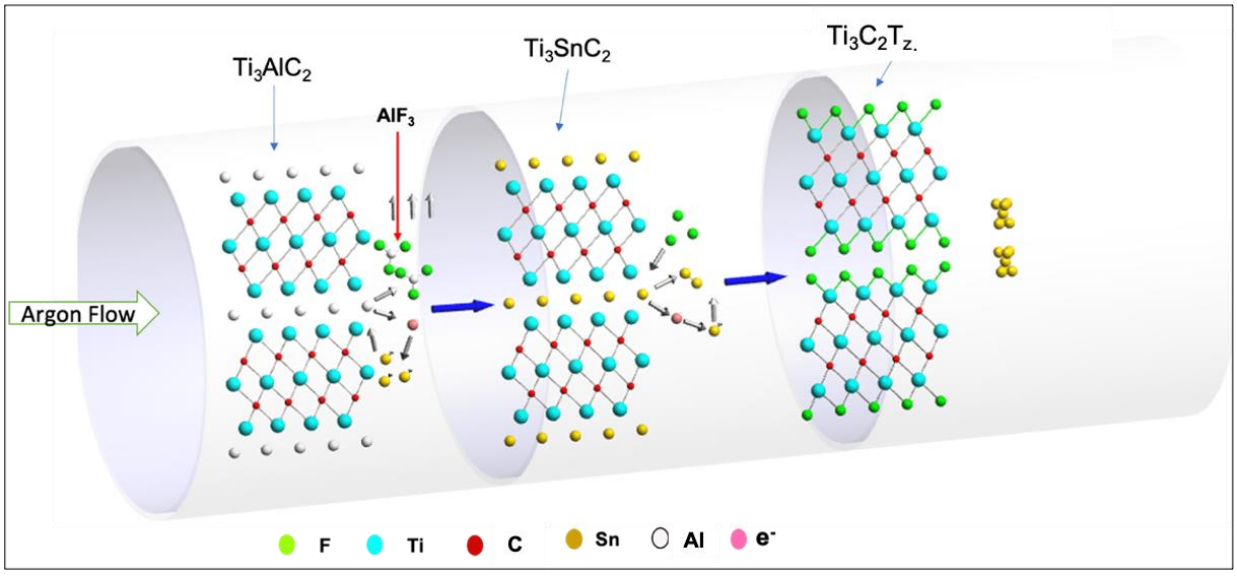

Figure 1. Schematic of the reaction setup used for molten salt etching in a tube furnace under argon flow to minimize the interference of oxygen during etching.

CHAPTER II

SYNTHESIS, PROPERTIES, AND APPLICATIONS OF MXenes

2.1 Introduction

In recent years, 2D nanosheets referred to as "MXenes" have caught the world's attention because of their wide compositional range and remarkable set of properties[1, 2, 12, 16-18]. MXenes are prepared by the selective etching of the A-layer element from a parent $M_{n+1}AX_n$ (or MAX) phase, where M is an early transition metal (Ti, V, Nb), A is an element from groups 13-16, and X is carbon or nitrogen (**Figure 2**). The general formula for MXenes is $M_{n+1}X_nT_z$ (n = 1-3), where T_z stands for the surface terminations, such as -F, -Cl, -OH, or -O, which are bonded to outer M layers on 2D nanosheets [10, 19]. Due to their material properties, such as metallic conductivity and hydrophilicity, MXenes have been used in wide range of applications in energy storage, catalysis, electromagnetic interference shielding, sensor, composites, and batteries [6, 9, 11, 20-24].

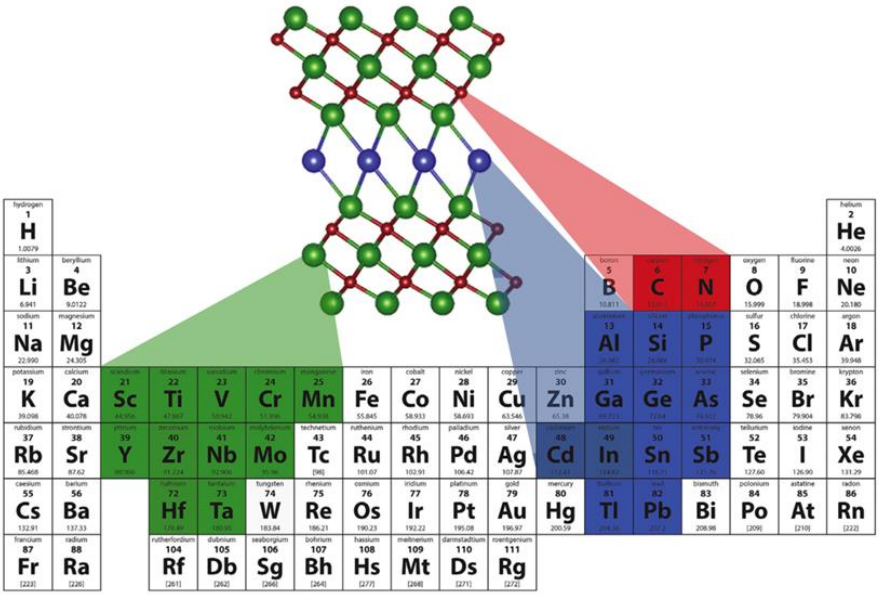

Figure 2. MAX phases $M_{n+1}AX_n$ forming elements[25]. (Reprinted with permission from Ronchi *et. al.*)

2.2 Synthesis

Since the discovery of $Ti_3C_2T_z$ in 2011, MXenes have been generally prepared by the selective etching of the A-layer in an aqueous solution containing fluoride ions such as aqueous hydrofluoric acid (HF). Other methods include the use of a mixture of hydrochloric acid (HCl) and fluoride salts (such as LiF), or ammonium bifluoride $(NH_4)HF_2$ [1, 26]. The significant drawbacks of HF-related methods are the inherent dangers of using HF, its waste management, scalability, and lack of versatility in etching MAX phase [13].

Sun *et al.*, in 2017, proposed an electrochemical method without the use of F for the delamination of Ti_2C in a dilute aqueous HCl electrolyte[14]. They constructed a two-electrode system with bulk Ti_2AlC as anode and cathode. After etching, the Ti_2AlC electrode was washed with DI water to remove the electrolyte residues. However, scaling up selective electrochemical etching methods to large production volumes may be a challenging task.

Li et al., in 2018 reported, a way to obtain $Ti_3C_2T_z$ MXene from the Ti_3AlC_2 MAX phase, assisted by sodium hydroxide (NaOH)[27]. In this method, the hydroxide anions (OH) attack the Al layers, which results in the formation of Aluminum hydroxides. The generated $Al(OH)_4$ are then dissolved in alkali solution (27.5 M NaOH) and the exposed Ti atoms are terminated by OH or O. The problem of confinement of newly formed aluminum hydroxide into the lattice from the Ti layers and failure react anew with the hydroxide ions is eliminated by the application of a series of hydrothermal temperatures and concentrations of NaOH water solutions under an argon atmosphere.

Despite various methods to make MXene, there is a need to minimize the dangers and challenges of the HF-related etching techniques, process time, and scalability of MXenes at an industry level. In order to achieve these issues, researchers invented molten salt etching method to produce MXenes [15, 28-30]. Molten salt etching method reduces the etching process time by half as compared to traditional acid etching method. The molten salt method is less hazardous than traditional methods because HF is not involved. In addition, this reaction is completely contained during the etching process and requires little intervention or exposure to the chemicals, which is not the case with HF-related methods. However, this method has not yet produced MXenes that could be dispersed in water, thus preventing there wider processing and application.

In 2016, Urbankowski *et al.* first reported the use of molten salts to create nitride MXenes by etching parent MAX phase in a eutectic mixture of fluoride salts[15]. Later, Li *et al.* synthesized $Ti_3C_2T_z$ MXene with an element replacement approach, where Al in MAX phase is first replaced

by Zn, followed by the removal of Zn; to do so, they performed a reaction between Ti_3AlC_2 with $ZnCl_2$, a Lewis acid, at 550 °C [28]. The final product is a Cl-terminated $Ti_3C_2T_z$ clay with typical accordion structure, but no water dispersible and separated nanosheets were reported.

In 2020, Li *et al.* used redox-controlled A-site etching in Lewis acid molten salts to synthesize MXenes from several MAX phase precursors with Si, Zn, and Ga as the A element. In that work, they mixed the MAX phase powder with a combination of salts such as $CuCl_2$, NaCl, and KCl and heated the mixture to 750 °C for 24 h inside an alumina tube under flowing argon [29]. They were able to create $Ti_3C_2T_z$ clay, but they were unable to delaminate it into single layer nanosheets like the previous paper.

Kamysbayev *et al.* reported the ability to tailor the surface groups of MXenes using $CdBr_2$ and $CdCl_2$ molten salts and are also the only group to date to go beyond etched MXene "clays" and produce dispersed $Ti_3C_2T_z$ nanosheets [30] but in N-Methylformamide (NMF), not in water. They also found that after the initial etching of the MAX phase, the MXene terminal groups predominantly contain the halogen group of the salt. In this work the authors were able to exchange the terminal groups by using a mixture of molten salts. The molten salt method of etching is promising for its versatility in the wide variety of etchable MAX phases and its ability to select the terminal groups of the MXene.

2.3 Properties

2.3.1 Mechanical Properties

The surface terminal groups of the MXene show significant differences in their mechanical

properties. Bai *et al.* has reported a stronger interaction between the O terminations and Ti atoms than in the F or OH terminated of Ti_2C and Ti_3C_2 MXenes[31]. The higher stiffness of O-terminated MXene is attributed to the higher bond strength of Ti-O as compare to Ti–OH and Ti–F. The bond strength of the Ti-C bond considerably affects the electric properties of MXene. Zha *et al*. reported that O-terminated MXenes should be used for applications regarding structural materials, supercapacitors, and so on, due to their higher mechanical strength[32].

2.3.2 Electronic Properties

The most important electronic property of MXene is their high electronic conductivity which is attributed to the presence of metallic bonding of transition metals. In addition to that the high conductivity of pristine or bare MXene is contributed by presence of larger number of d orbitals of the transition elements around and above the Fermi energy level.

The conductivity of MXene is generally tuned by the modification of terminal groups of MXene and there are different ways to modify the terminal groups of MXene. Annealing method is generally used to modify the terminal groups of MXene nanosheets[33, 34]. The annealing of MXene involves the heating of MXene at an elevated temperature under inert atmosphere. Annealing process results into a removal of terminal groups of MXene surface and the formation of bare MXene (no terminal groups on MXene surface) and bare MXene generally exhibit a metallic behavior. The reason behind the variation of conductivities is attributed to differences on the a) concentration of defects, b) delamination yield, c) d spacing between MXene nanosheets, d) lateral size of MXene flakes[35].

2.3.3 Optical Properties

MXene thin films of thickness about 15 nm possess an excellent optical transmittance (>80%) as compared to the reduced graphene thin films. MXene films formed by layer-by-layer method has lowest optical absorption compare to reduced graphene and sputtered MXene[36, 37]. These characteristics are important for the enhancement if transparent conductor efficiency and achieving greater illumination of active materials, such as displays and photovoltaic cells. There still some optical related features, such as luminescence efficiency, emission colors, plasmonic and non-linear optical properties need to be researched to use MXene in optical applications.

2.4 Applications:

2.4.1 Energy Storage

Depletion of fossil fuels and rising energy consumption led to increasing interest in renewable energy sources, storage and conversion systems such as batteries and supercapacitors. Recent advancements in the use of different electrochemical active materials like sp^2 hybridized carbon materials, graphene, fullerene and carbon nanotubes has resulted in enhanced energy storage compared to traditionally used graphite due to their high electrical conductivities and large surface area[38-44]. MXenes has attracted the extensive research interest for energy storage application due to their high intrinsic surface area, electrical conductivity, proton exchange and mechanical strength[3, 7, 45, 46].

2.4.1.1 Supercapacitors

Supercapacitors comes under the category of electrical energy storage systems that store electricity

by forming a double layer at the interface of electrode and electrolyte. In this case, the power densities are superior to those of dielectric capacitors and other electrochemical energy storage devices. Depending on the actual charge storage mechanism, supercapacitors are classified into three major types (i) electric double layer capacitors (EDLC), (ii) pseudocapacitors and (iii) asymmetric hybrid capacitors[41, 47-58].

The multilayered $Ti_3C_2T_z$ showed the capacitance of 324 F/cm^3 in KOH basic solution while multilayered $Ti_3C_2T_z$ showed the capacitance of 940 F/cm^3 (scan rate 2mV/s) when exposed to acidic solutions (H_2SO_4)[22, 59]. $Ti_3C_2T_z$ showed pseudocapacitive mechanism in an acid solution (H_2SO_4), only electric double layer capacitance is observed in alkaline electrolytes, which downgrades their performances. The difference in the behaviors of capacitance of MXene based supercapacitors in acidic and basic electrolyte is attributed to the difference in charge-discharge mechanisms. The substitution of -F terminal groups by -O terminations showed enhanced capacitive performance[60]. The different MXene synthesis routes generate the MXenes with various terminal groups and the variable surface terminal groups give rise to a variable capacitive performance due to their interaction with electrolyte.

2.4.1.2 Batteries

Li-ion batteries has caught the attraction of researchers due to their high energy densities, long cycling performance. The current system of graphite anode/$LiCoO_2$ spinel cathode is used majorly in commercial Li-ion batteries. However, graphite anodes have low storage capacities for the

future energy demand. Therefore, it is necessary to develop an electrode material with high energy density for the next generation of Li-ion batteries. MXene and its composites have showed a enhancement in energy density and power density for battery application, due to their high electronic conductivities, specific surface areas, low diffusion barrier, and Li storage capacities with low circuit voltage[6, 7, 42, 46, 61].

The presence of terminal functional groups over the surface of MXene effects metallic ions adsorption, intercalation chemistry, storage capacity and operating potential. Therefore, selection of MXene synthesis process is very much important. Generally, the presence of terminal functional groups increases the diffusion barrier. For example, the theoretical lithium-ion capacity of titanium Ti_3C_2 increased by five times after the removal of hydroxyl terminal groups.

2.4.1.3 Photovoltaic Devices

Recently, MXenes have been proved to be a potential candidate in the field of photovoltaics and energy storage due to their high transmittance, metallic conductivity, and tunable work function. The increase in the worldwide consumption of energy has influenced the discovery and research into solar cell technology. Perovskite hybrid solar cells serve as an excellent choice for this application, and within half a decade there has been tremendous increase in the power conversion efficiency up to 20%. However, a rapid property deterioration in organic-inorganic perovskite hybrid solar cell devices occurs due to the instability of the organic layers present in them, which promotes the carrier recombination at the electrode interface. To combat this problem, MXenes are widely used as a part of perovskite solar cell devices. MXene integration into the solar cell both as charge transport materials and absorber layer additives is also explored by the

researchers[62]. There has been a variation of photovoltaic (PV) properties of the fabricated perovskite solar cell because of variable electronic properties and bandgap of the different MXenes (Ti, Va or Ni based).

2.4.2 Actuators

The layered structure of MXene enables the intercalations of many cations into the layered structure, thereby changing the volume, which allows for actuation in response to electrical stimuli. The reason behind the intercalation of cations is the negatively charged surface (Negative ζ potential of MXene dispersion) and polar functional groups of MXene. The $Ti_3C_2T_z$ MXene can be intercalated using various cations (Li^+, Na^+, Mg^{2+}, K^+, NH^{4+}, and Al^{3+}) as reported by researchers[63-71]. However, since cation intercalations are limited to electroactive ionic actuators, ionic liquid intercalation could be used for their dry counterpart that can function in an open-air environment. When MXenes are dipped into ionic liquids, applying negative potential produces positive strain (i.e., increase in volume) due to the intercalation of larger size cations, whereas a positive potential stimulates negative strain (decrease in volume) as a result of the intercalation of small size anions layered structure.

Since MXenes have very strong EM absorption and can exhibit up to 100% light to heat conversion efficiency, they are an attractive choice for photothermal actuators [8, 69, 70]. Additionally, MXenes can be used to fabricate actuators that are highly sensitive to humidity, as the hydrophilic functional groups contribute to the interaction between the nanosheets and adsorbed water molecules, and thus enlarge the d-spacing of the MXene.

2.4.3 Polymer Composites

MXenes are ideal material for polymer composite because of their high electrical conductivity, robustness, and thermal stability[25, 72]. Though, optimization of the polymer and MXene composites are required to achieve multifunctional capabilities or properties. These composites can be fabricated by simple and low-cost methods, into fibers, films, or 3D printed structures[25]. These polymer-MXene nanocomposites exhibit high photothermal conversion efficiency, electron sensitivity, and mechanical stability[25, 31, 73].

In the field polymer composites, MXenes are primarily used to improve the mechanical properties and electrical conductivities of polymer matrixes. For example, $Ti_3C_2T_z$ – polydiallyldimethylammonium chloride (PDDA) or polyvinyl alcohol (PVA) or polyacrylamide (PAM) based composites showed excellent values of electrical conductivity[74, 75]. Additionally, Vanadium based smart composites showed 10 times increase of electrical conductivity with temperature increases from 15 to 45 °C[76]. Also, in the case of mechanical properties, $Ti_3C_2T_z$-PVA-CNC (cellulose nanocrystals) fibers reported the increase in Young Modulus from 392 to 855MPa compared to polymer matrix[77]. Recently, the addition of 0.5wt% $Ti_3C_2T_z$ offered the increase in the yield stress by 70% in Polyurethan (PU)matrix[78].

However, it must be noted MXenes incorporation influences the structure and crystallization rate of the polymer matrix[79, 80]. Huang *et al.* studied the $Ti_3C_2T_z$ - polyethylene oxide matrix and they used in solid polymer electrolytes[79]. Huang *et al*. have reported the two competing effects upon the crystallization rate. They stated that at low concentrations, there is an increase in the crystallization rate due to the increase in sites available to heterogeneous nucleation, whereas at

high concentration, MXenes form a rigid network, which restricts the spherulite growth and crystallization rate.

CHAPTER III

EXPERIMENTAL SECTION AND CHARACTERIZATION OF MXene

3 Experimental Section

In the following work, we develop the first-ever molten-salt method to create colloidally stable $Ti_3C_2T_z$ nanosheets in aqueous solution. This is the first reported use of SnF_2 as the etchant to form fluorine terminated $Ti_3C_2T_z$ nanosheets. Using SnF_2 as the etchant produces an extremely open $Ti_3C_2T_z$ clay structure. A KOH wash of the clay was necessary to replace some of the -F terminal groups with hydrophilic -OH groups that promoted the formation of a stable aqueous dispersion.

3.1 Materials

The elemental powders used to prepare parent MAX phases were titanium (Alfa Aesar, -325 mesh, 99%), aluminum (Alfa Aesar, -325 mesh, 99.5%), and graphite (Alfa Aesar, 7-10 micron, 99%). The bucky paper used were supplied by Pall Laboratory. Tin fluoride (SnF_2) used were supplied by Acros Organics. The Potassium Hydroxide (KOH) pellets and Dimethyl Sulfoxide (DMSO) were ordered from Sigma Aldrich.

3.2 Experimental Methods

Synthesis of Ti_3AlC_2 MAX phase: Pressureless reaction sintering was used to synthesize parent MAX phases for etching. For Ti_3AlC_2, elemental powers powders of titanium, aluminum, and graphite were scaled in the molar ratio of 3:1.2:1.95, respectively. The powders were milled in a jar rolling mill with 35 mm high-density ZrO_2 cylinders at 300 RPM for 12 hours to prepare a homogenous mixture. After mixing, the elemental powders were loaded into alumina crucibles,

which were inserted into diameter alumina tube vacuum furnace (MTI Corporation, GSL-1600X-50-UL). Once sealed, a vacuum was pulled on the tube to an ultimate pressure of 10^{-3} torr, followed by a short purge with ultra-high purity argon (UHP Ar). This step was repeated three times to ensure the removal of air. While maintaining a constant flow of UHP Ar, the samples were heated at a rate of 10 ºC/min to 1510 ºC and dwelled for 4 hours. After dwelling, the samples cooled naturally. The resulting bulk MAX phase was crushed using an alumina mortar and pestle and were sieved through a 325-mesh sieve to obtain powders of a suitable size for etching.

Synthesis of $Ti_3C_2T_z$: The $Ti_3C_2T_z$ was prepared by a reaction between the MAX phase precursor (Ti_3AlC_2) and SnF_2. For synthesizing $Ti_3C_2T_z$, a mixture of powder with a molar ratio of Ti_3AlC_2/SnF_2 = 1:6 was used as a starting reaction material. The starting material was mixed thoroughly by stirring with a glass rod. Then, the mixture powder was transferred into an alumina boat. The alumina boat was loaded into a tube furnace (Thermo Scientific Lindberg/Blue M TF55030A) and heated for 6 hours at 550 °C under flowing UHP Ar. After the reaction, the product was washed with 0.1M potassium hydroxide (KOH) to dissolve the excess salt and subsequently washed with deionized water 4 times to remove the residual KOH. The $Ti_3C_2T_z$ clay was then redispersed into DMSO for intercalation for 20 hrs., and then washed with water 3-4 times to remove DMSO. Sediment was then redispersed in water and bath sonicated for 60 min to delaminate the nanosheets. Finally, the bath sonicated dispersion is centrifuged for 20 min on 3500 RPM. $Ti_3C_2T_z$ nanosheets obtained in the supernatant were freeze-dried for further characterization.

Preparation of supercapacitor electrodes: $Ti_3C_2T_z$ clay (the product after etching and water washing but before intercalation, sonication, and centrifugation) and $Ti_3C_2T_z$ nanosheet powder were used as the active material to prepare the supercapacitor electrode. The electrodes are composed of 80 wt % active material, 10 wt % carbon black (Alfa Aesar, 99.9%), and 10 wt % Polyvinylidene fluoride (PVDF) binder. PVDF is used as a binder. The active material, carbon black and binder were dispersed in N-Methyl-2-Pyrrolidone (NMP). The supercapacitor electrode is constructed by doctor-blade onto a flat carbon paper surface. The electrodes were then dried for 48 h at room temperature. Before electrochemical characterization, the electrodes were immersed in the electrolyte solution for 0.5 h to enhance the electrolyte diffusion into the material bulk.

3.3 Characterization

Scanning Electron Microscopy (SEM): The morphologies of $Ti_3C_2T_z$ clay and nanosheets were observed with a FEI Quanta 600 field-emission scanning electron microscope. For imaging, the vigorously mixed dispersions of MXenes were freeze-dried for 24 h. The acceleration voltage used in the imaging was 5 kV. The SEM samples were prepared by drop-casting the diluted dispersion of $Ti_3C_2T_z$ on a silicon wafer and letting it dry in a vacuum overnight.

X-ray Diffraction (XRD): XRD patterns of dried $Ti_3C_2T_z$ were obtained using Bruker D8 powder X-ray diffractometer fitted with LynxEye detector, in a Bragg Brentano geometry with CuKa (l = 1.5418 A) radiation source. The XRD was performed with a step size of 0.02° and a scan rate of 1.5 s per step. The $Ti_3C_2T_z$ samples were freeze-dried before the XRD. A zero-background sample holder was used in all the tests.

Energy Dispersive Spectroscopy (EDS): Elemental composition analysis was done using an Oxford EDS detector on FEI Quanta 600 SEM, and results were analyzed using AZtec software by Oxford Instruments. The powdered sample was exposed to a beam, and imaging was done at 20 kV acceleration voltage.

Transmission Electron Microscopy (TEM): 3 microliters of $Ti_3C_2T_z$ dispersion in water was drop cast on a holey carbon grid, and the grid was pre-treated by glow-discharging to make it hydrophilic. The excess solution was wiped off with a filter paper and then air-dried. The samples were imaged by using an FEI Tecnai F20 transmission electron microscope operating at 200 kV.

Atomic Force Microscopy (AFM): $Ti_3C_2T_z$ dispersion was again diluted with water and drop-cast on a freshly cleaved mica substrate. The mica substrate was allowed to dry overnight in a vacuum oven at 30°C. The samples were imaged using Bruker Dimension Icon AFM for scanning probe microscopy, and height profiles were obtained with a MultiMode™ scanning probe microscope.

UV-Vis Spectroscopy: UV–vis measurements were done using Shimadzu UV−vis 2550**.** The sample used for UV Vis absorption spectra was $Ti_3C_2T_z$ dispersion in water with a 0.4 mg/ml concentration. The readings were taken multiple times to achieve maximum accuracy.

Radio Frequency (RF) heating: A stationary, fringing field applicator fabricated in –house by laser-etching copper traces on an FR4 substrate was used for this experiment. The copper traces with spacing 4 mm act as capacitors, resulting in a fringing field coming out-of-the-plane of the applicator. The RF field was generated using a RIGOL DSG815 signal generator, which were then

amplified using a PRANA GN 500 amplifier and supplied to the applicator via a coaxial cable. The frequency was hand-tuned to obtain maximum heating rate, and temperature vs. time was observed at that frequency for powers 1 and 10 W. The sample used for the RF study was a buckypaper, which was made by vacuum filtration of MXene dispersion using Supor Polyethersulfone Membrane (Pall Laboratory).

Dynamic Light Scattering (DLS): The hydrodynamic diameters of aqueous $Ti_3C_2T_z$ nanosheets were determined at ambient temperature by DLS at a scattering angle of 90º using a Zetasizer Nano ZS90 from Malvern Instruments. The colloidal aqueous dispersion of $Ti_3C_2T_z$ nanosheets was diluted to a concentration of around 0.009 mg/mL before making the measurements.

ζ Potential Measurement: ζ potential of $Ti_3C_2T_z$ nanosheets in water were measured at ambient temperature using the Zetasizer Nano ZS90 from Malvern Instruments and the appropriate capillary cell, DTS 1070, from Malvern Instruments. The $Ti_3C_2T_z$ nanosheets dispersion was diluted to a concentration around 0.009 mg/mL before measurements to ensure consistency. Each test was repeated 2 times, and an averaged value was derived to ensure accuracy.

Cyclic Voltammetry (CV): The electrochemical properties of the $Ti_3C_2T_z$ were investigated with cyclic voltammetry (CV) and chronopotentiometry by a Gamry Reference 3000™ potentiostat. The three-electrode testing was carried out using AgCl as a reference electrode and platinum wire as the counter electrode. A two-electrode system was made using a Swagelok cell. The supercapacitor cell was assembled with two electrodes and one separator constructing a symmetric sandwich structure. A Celgard™ separator (3501 Coated PP) is used. The electrolyte used for analysis is 1 M H_2SO_4.

CHAPTER IV

RESULTS AND DISCUSSION

4 MXene Formation

4.1 Molten Salt Etching of MXene

The molten salt etching procedure was carried out as follows: A mixture of Ti_3AlC_2 and Tin fluoride (SnF_2) was heated for 6 hours, resulting in the formation of $Ti_3C_2T_z$ clay with some Sn spheres. After etching, the $Ti_3C_2T_z$ clay was washed with Potassium hydroxide (KOH) solution to dissolve and remove the excess or unreacted SnF_2 crystals. KOH-washed $Ti_3C_2T_z$ clay was intercalated with dimethyl sulfoxide (DMSO) and then washed with water to remove DMSO. After intercalation, the $Ti_3C_2T_z$ clay was delaminated by bath sonication, and the dispersion of delaminated $Ti_3C_2T_z$ is centrifuged; this resulted in a stable dispersion of $Ti_3C_2T_z$ nanosheets. The tube furnace set up and processing schematic is shown in **Figure 1 and Figure 3 respectively.**

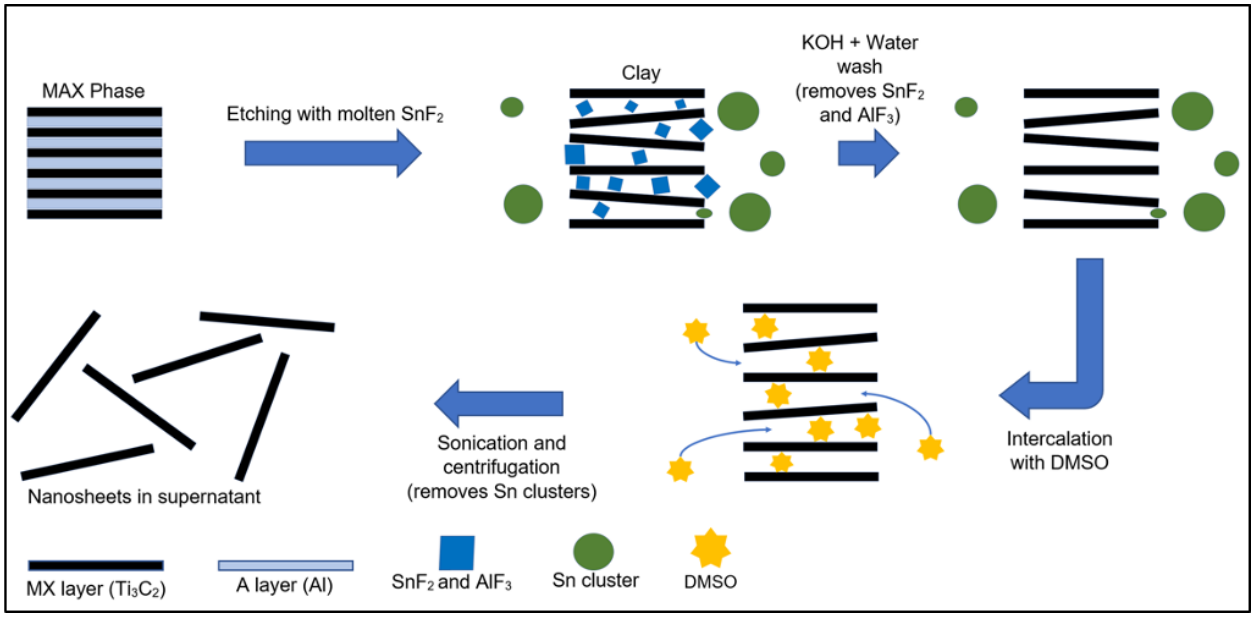

Figure 3. $Ti_3C_2T_z$ processing schematic, which clearly shows every step need to be followed to get $Ti_3C_2T_z$ dispersion.

After heating the mixture of Ti_3AlC_2 and SnF_2 with a mole ratio of 1:6 at 550 ºC for 6 hours, a $Ti_3C_2T_z$ clay was formed, along with Sn spheres present. The SEM images **(Figure 4b)** show the typical "accordion" structure of $Ti_3C_2T_z$ clay, indicating successful etching of the A element, with clear expansion between the basal planes. However, an unusual feature of that $Ti_3C_2T_z$ clay (**Figure 4**) is the presence of crystalline structures intercalating the layers. Based on the EDS data shown in **Figure 5**, the crystalline structures are likely SnF_2 and AlF_3. We hypothesize that the SnF_2 diffused in between the layers during etching, and AlF_3 formed between the layers. The large spheres that are present are made of Sn that agglomerates as F is consumed from SnF_2 is used up during the etching. The EDS mapping and chemical composition of $Ti_3C_2T_z$ clay is shown in **Figure 5** and **Table 1**, confirming successful removal of the A-layer form the parent MAX phase.

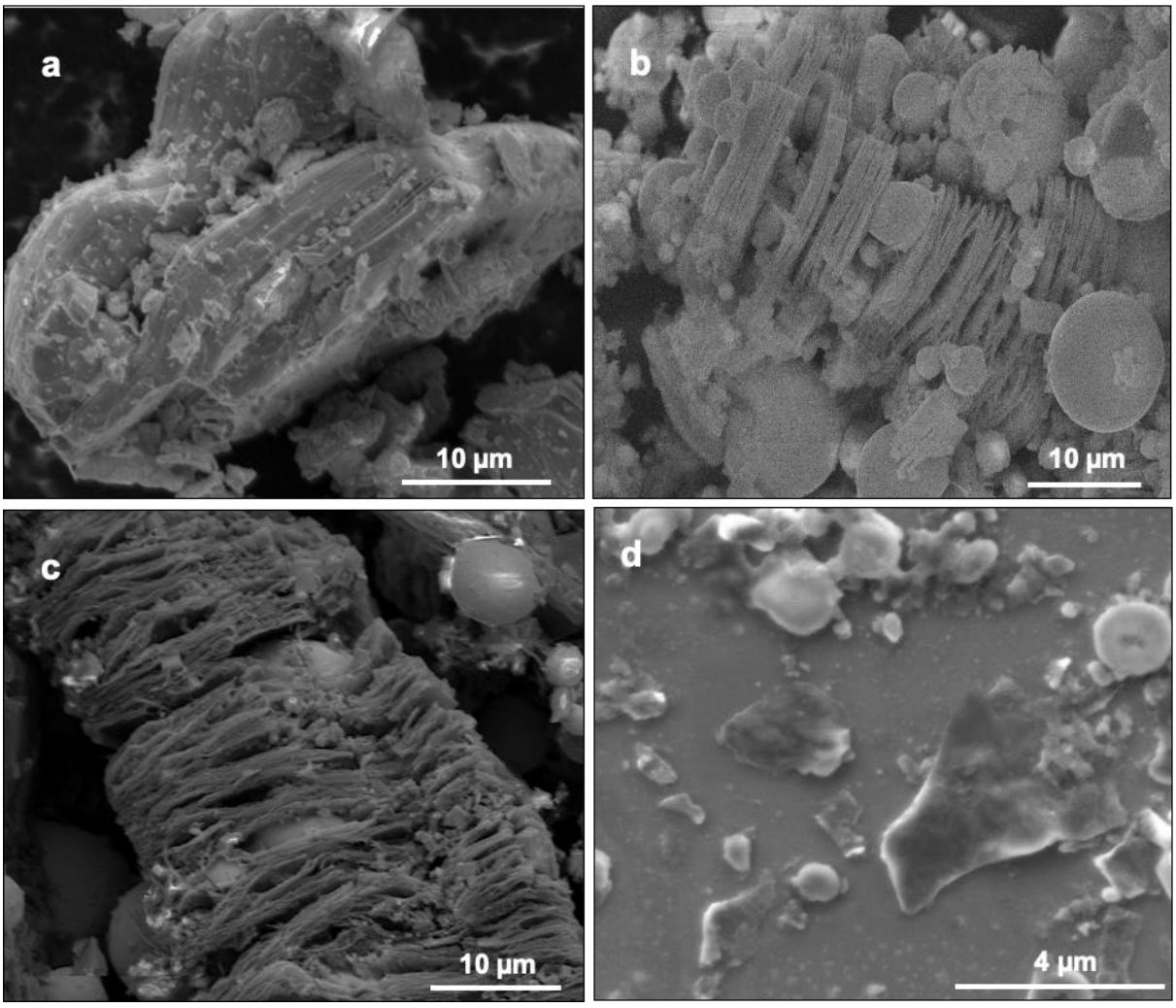

Figure 4. SEM Image of: (a) parent Ti_3AlC_2 MAX phase; (b) $Ti_3C_2T_z$ before KOH wash (freeze dried); (c) $Ti_3C_2T_z$ after KOH wash (freeze dried); (d) $Ti_3C_2T_z$ nanosheets drop-cast from aqueous dispersion.

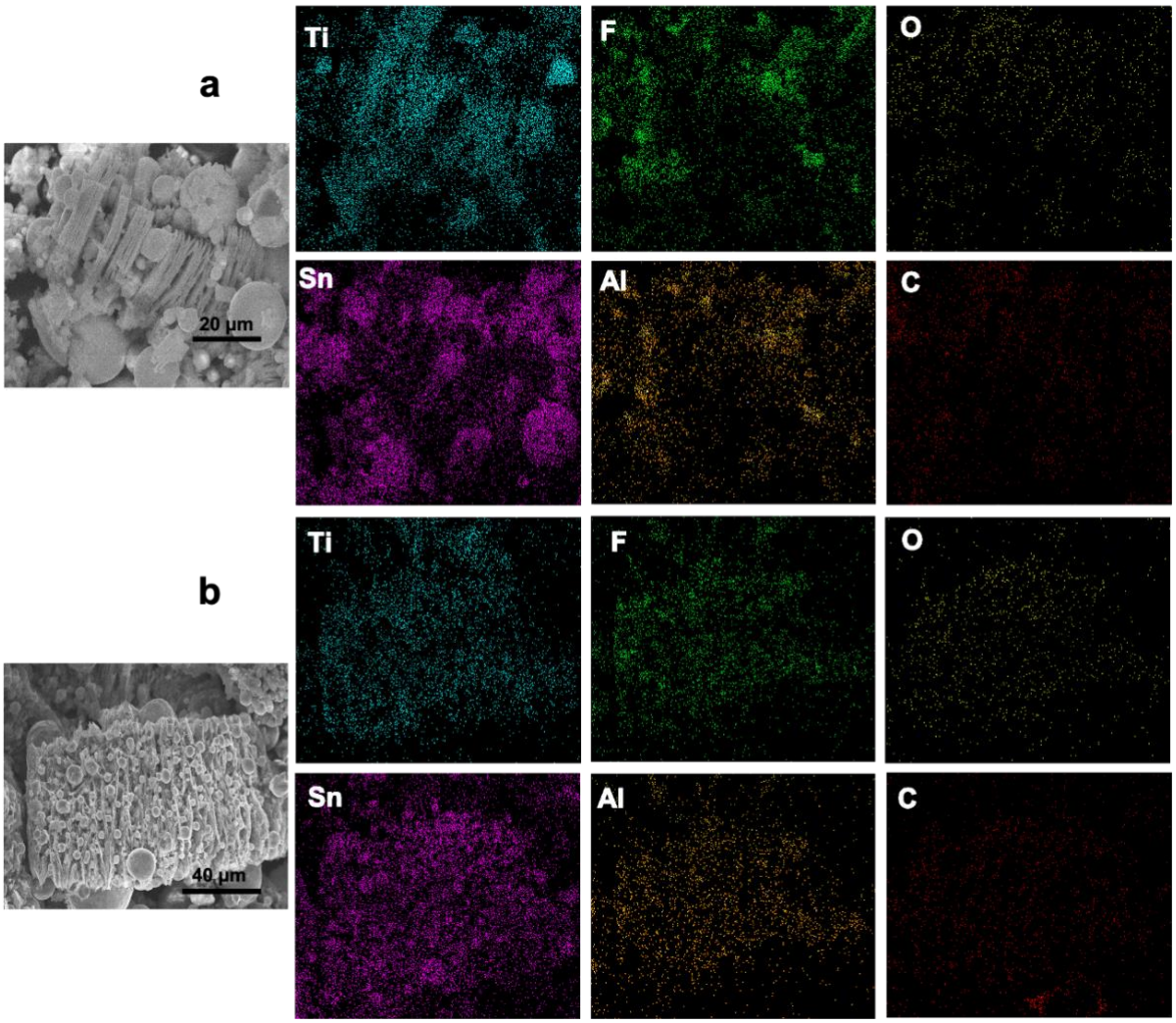

Figure 5. EDS mapping of $Ti_3C_2T_z$ clay a) before KOH washing b) after KOH washing.

Without the KOH wash step, we could not produce a stable $Ti_3C_2T_z$ nanosheet dispersion; we hypothesized that the colloidal instability is likely due to a lack of -OH terminal groups, which are present on $Ti_3C_2T_z$ nanosheet synthesized by conventional HF etching technique. With this in mind, the $Ti_3C_2T_z$ clay was washed with 0.1M KOH solution for 2 hours to add these -OH terminal groups and allow for dispersibility. In addition, the KOH wash also dissolves and remove the excess SnF_2 entrapped inside the $Ti_3C_2T_z$ clay **(Figure 5)**. The EDS mapping and chemical composition of

$Ti_3C_2T_z$ clay before and after KOH washing is shown in **Figure 5** and **Table 1**, which confirms the removal of unreacted or excess SnF_2 based on the decrease in fluorine content.

	MAX phase Ti_3AlC_2	**MXene Before KOH wash**	**MXene After KOH wash**
Element	% Weight	% Weight	% Weight
C	14.5	8.25	9.24
O	-	6.64	11.00
F	-	37.43	33.43
Al	16.3	2.90	2.86
Ti	69.1	11.97	8.02
Sn	-	31.97	35.19

Table 1. EDS data which shows the elemental composition of the $Ti_3C_2T_z$ clay before and after KOH washing corresponding to Fig. 4. The highlighted red shows the reduced percentage of aluminum compared to MAX phases which indicated the successful etching.

KOH-washed $Ti_3C_2T_z$ clay was then intercalated with DMSO for 20 hours and washed with water 3-4 times to remove DMSO**.** After intercalation, the $Ti_3C_2T_z$ clay was delaminated by bath sonication for 1 hour. The resulting mixture was then centrifuged. This results in the formation of stable dispersion of $Ti_3C_2T_z$ nanosheets **(Figure 4d)** in the supernatant (**Figure 6b**)**.** The supernatant contained some Sn spheres along with the $Ti_3C_2T_z$ nanosheets; in order to remove these impurities, a two-stage centrifuge method was used (**Figure 6a)**. The two-stage centrifuge method consists of

a light centrifuging at 5000 rpm for 10 minutes, and an additional heavy centrifuging of the supernatant at 9000 rpm for 20 minutes. The resulting $Ti_3C_2T_z$ nanosheets are colloidally stable with a negative ζ potential (-31.7 mV) and 359 nm particle size (measured by DLS).

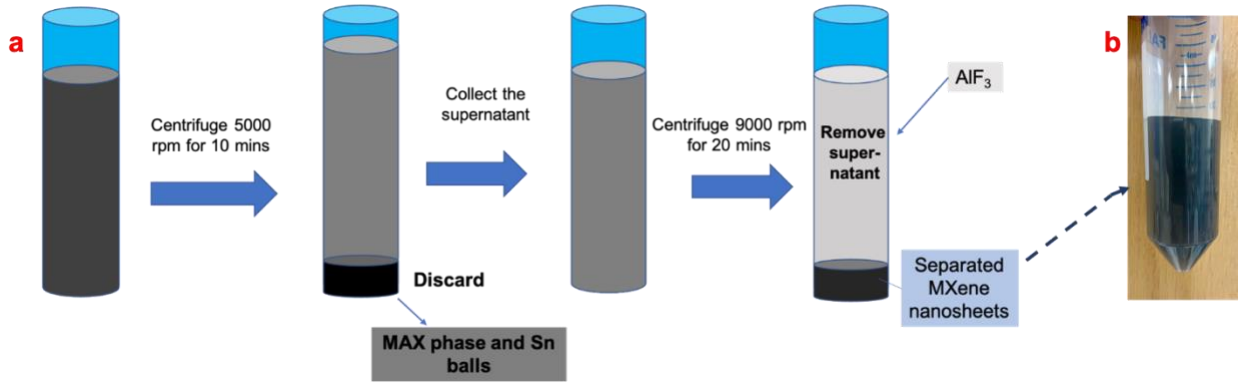

Figure 6. (a) Two-Stage centrifugation method used for the separation of $Ti_3C_2T_z$ from the Sn Spheres. This method helped to get rid of heavy MAX phase particles and other small unwanted particles from the supernatant. (b) Stable aqueous dispersion of Ti3C2Tz nanosheets with negative ζ potential.

The SEM and EDS mapping **(Figure 7)** indicate an elemental composition **(Table 2)** for few-layer $Ti_3C_2T_z$ and single-layer $Ti_3C_2T_z$ nanosheets of Ti/F/C = 28.6:17.5:14.1 (wt. %) and Ti/F/C = 18.4:18.7:9.9 (wt. %) respectively. Element mappings reveal that Ti, C, O, and F atoms are uniformly distributed throughout the entire structure (**Figure 7**), where F and O atoms are from the introduced –F, –OH, =O group. These functional groups are important for achieving high capacitance in aqueous electrolytes. Also, the reduction in the amount of Al (16.3 wt.% to 2.9 wt.%) compared to the parent MAX indicates the selective etching of Al.

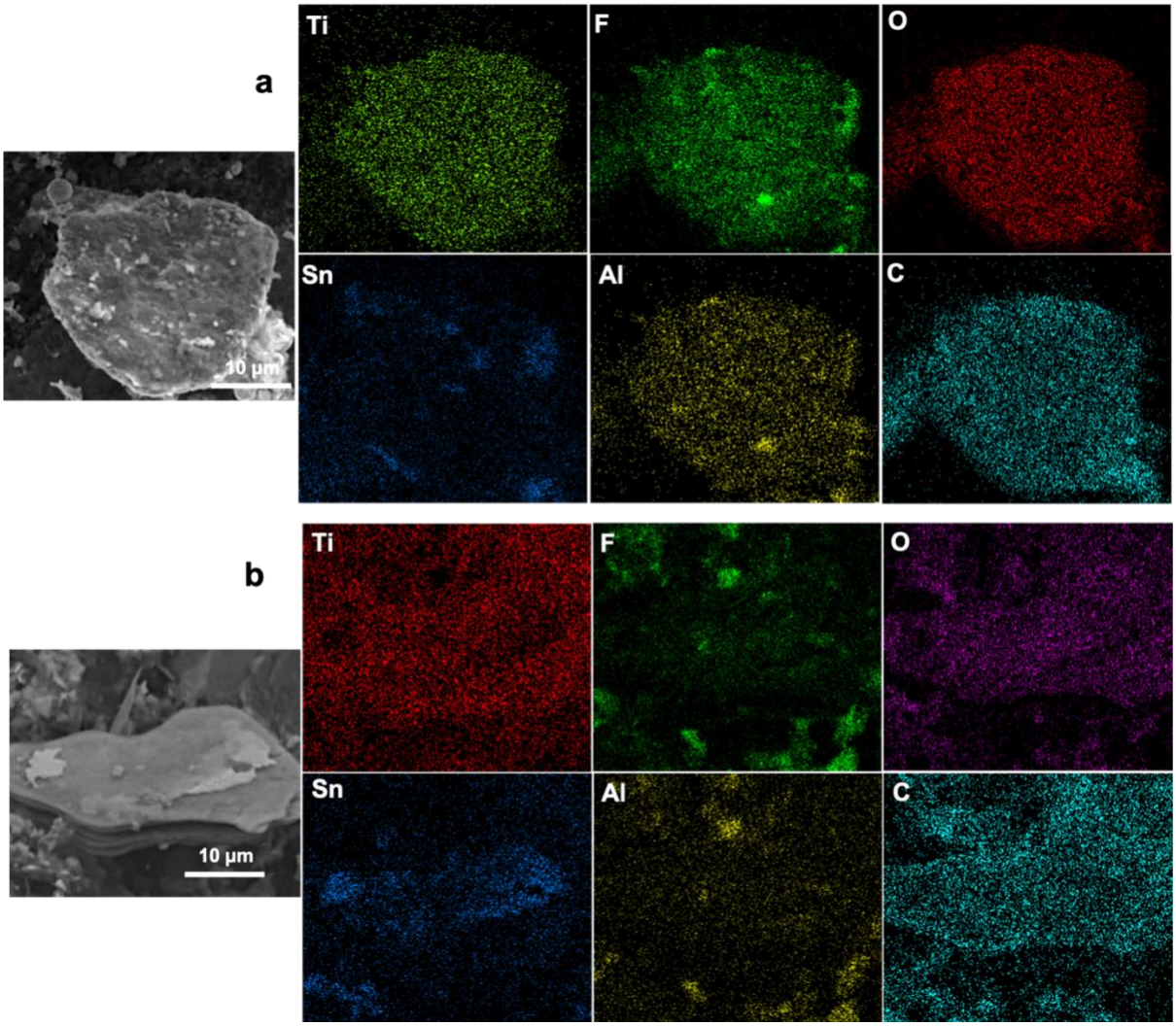

Figure 7. EDS of (a) Single-layer $Ti_3C_2T_z$ nanosheets; (b) few-layer $Ti_3C_2T_z$; we can clearly see the lower %wt. of Al, which indicates successful etching of Al from TI_3AlC_2.

$Ti_3C_2T_z$	**Multi-layer Nanosheet**	**Single Layer Nanosheet**
Element	% Weight	% Weight
Ti	28.6	18.4
Sn	18.3	22.4
F	17.5	18.7
O	14.5	17.9
C	14.1	9.9
K	1.7	9.0
Cl	0.2	4.0
Al	3.4	2.1

Table 2. Elemental composition of few-layered and single-layered $Ti_3C_2T_Z$ nanosheets obtained from EDS analysis corresponding to **Figure 7.**

Transmission electron microscopy (TEM) was used to determine the morphology of $Ti_3C_2T_z$ nanosheets. The TEM **(Figure 8a)** demonstrates the typical $Ti_3C_2T_z$ nanosheet morphology. The TEM image shows low contrast between the nanosheet and the background, indicating that this nanosheet is single- to few-layer. The UV-Vis spectra of the supernatant product are quite similar to that of conventional acid-etched MXene products (**Figure 8c**).

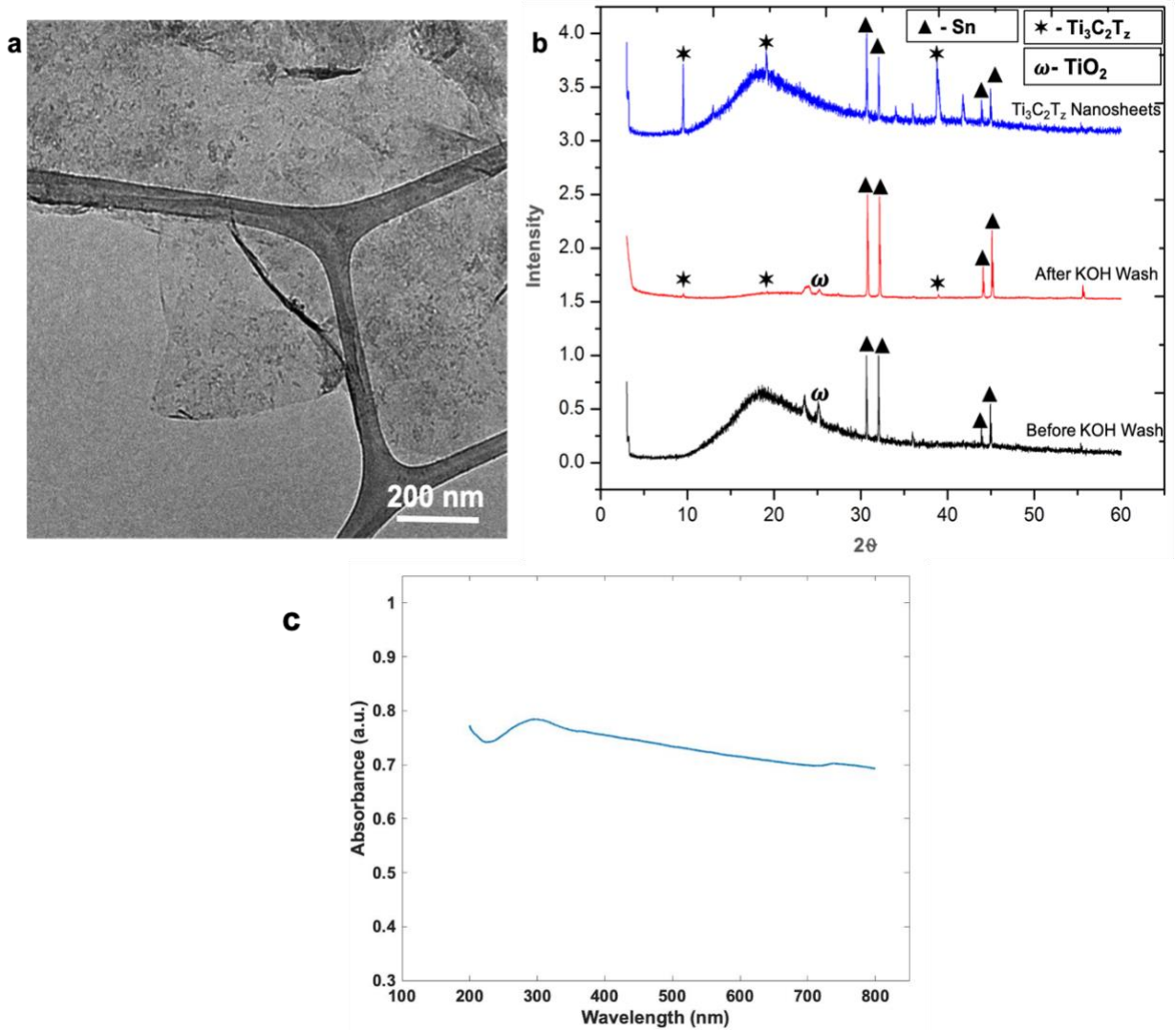

Figure 8. (a) TEM of $Ti_3C_2T_z$ nanosheet (supernatant); (b) XRD of $Ti_3C_2T_z$ clay before KOH washing, after KOH washing, and $Ti_3C_2T_z$ nanosheet (final supernatant). (c) UV–Vis absorption spectra of $Ti_3C_2T_z$ dispersion (0.4 mg/ml), which clearly resembles with the acid etched $Ti_3C_2T_z$ dispersion.

To Investigate the formation of $Ti_3C_2T_z$, we further performed X-ray Diffraction (XRD); **Figure 8b** shows the XRD patterns of $Ti_3C_2T_z$ clay before and after the KOH wash, along with the XRD of $Ti_3C_2T_z$ nanosheets from the supernatant. The non-basal plane peaks of Ti_3AlC_2 were not seen in the XRD, which indicates the successful etching of Al from Ti_3AlC_2. The characteristic peaks of $Ti_3C_2T_z$ are found at 9.4°, 19°, and 39°, which confirms the formation of $Ti_3C_2T_z$ [81]. The $Ti_3C_2T_z$

peak observed in the case of molten salt etching matches with the traditionally HF-etched $Ti_3C_2T_z$. The large peaks from 30°, 33°, 40°, and 46° are characteristic of Sn, which is a byproduct of the etching process described in the reaction mechanism (**Section 1**).

4.2 Section 1. Mechanism of MXene Formation

The formation of F-terminated $Ti_3C_2T_z$ is a two-step process as reported by Mian *et al.*[82], which we recapitulate here. **Step 1** involves the replacement of Al in Ti_3AlC_2 by Sn that results in the formation Ti_3SnC_2, which is an intermediate product in the formation of $Ti_3C_2T_z$ along with AlF_3 as a byproduct is generated. Also, as the reaction proceeds, Sn^{2+} ions form, which will intercalate into A site after removal of Al from Ti_3AlC_2.

Step 1

$$\mathbf{Ti_3AlC_2 + 1.5SnF_2 \longrightarrow Ti_3SnC_2 + AlF_3\,(g) + 0.5Sn}$$

I. $Ti_3AlC_2 + 1.5SnF_2 \longrightarrow Ti_3C_2 + 1.5Sn + AlF_3$

II. $Ti_3C_2 + Sn \longrightarrow \mathbf{Ti_3SnC_2}$

The formation of F-terminated $Ti_3C_2T_z$ depends on the ratio of the Al-MAX phase to SnF_2. The ratio of the Al-MAX phase to SnF_2 used in this study is 1:6. The exact mechanism behind the formation of $Ti_3C_2T_z$ was not clearly stated in the study by Mian *et al.* [82].

The formation of F-terminated $Ti_3C_2T_z$ from an intermediate product $\mathbf{Ti_3SnC_2}$ is represented in **Step 2**, which is further subdivided into three steps. Previous research indicated that the redox reaction between Sn and Sn^{2+} results in the dissolution of Sn into a molten SnF_2. The weakly bonded Sn atoms in Ti_3SnC_2 were easily removed from the A-site and dissolved into a molten salt SnF_2.

The F^- anions spontaneously intercalated into the A-site plane of Ti_3C_2 and bonded with specific site of Ti_3C_2 to form more stable F- terminated $Ti_3C_2T_z$.

Step 2

$$\mathbf{Ti_3SnC_2 + SnF_2 \longrightarrow Ti_3C_2F_2 + 2Sn}$$

I. $Ti_3SnC_2 + Sn^{2+} \longrightarrow Ti_3C_2 + Sn_2^{2+}$

II. $Ti_3C_2 + F^- \longrightarrow Ti_3C_2F_2 + 2e^-$

III. $Sn_2^{2+} + 2e^- \longrightarrow 2Sn$

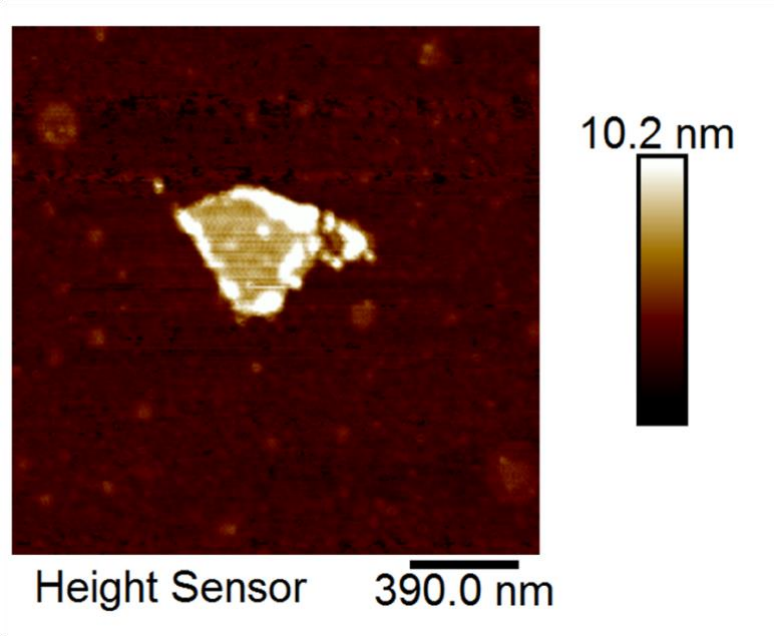

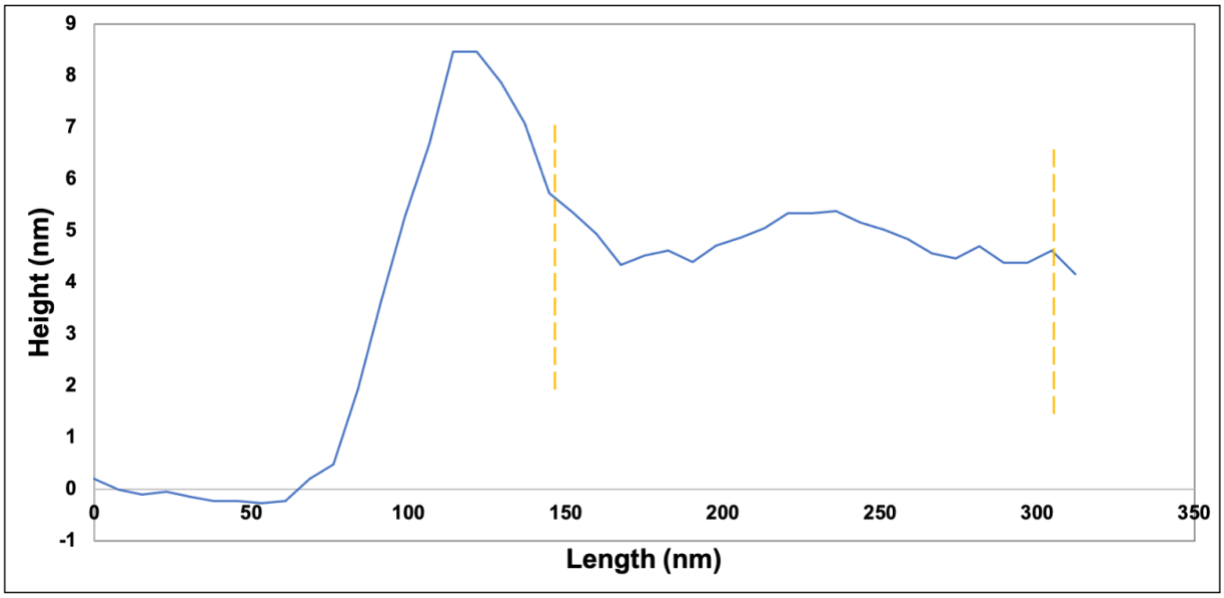

Figure 9. AFM image of $Ti_3C_2T_z$ nanosheet and corresponding height profile. $Ti_3C_2T_z$ dispersion was again diluted with water and drop-cast on freshly cleaved mica substrate. The concentration of sample used for AFM was 0.006 mg/ml.

A typical AFM image of the $Ti_3C_2T_z$ nanosheets is presented in **Figure 9** showing typical nanosheet thicknesses of 4-5 nm. The produced nanosheets are electrically conductive; the vacuum-filtered film showed a conductivity of 706 S/m. We also confirmed these conductive nanosheet films' ability to heat in response to radio frequency fields, similar to our prior paper (**Figure 10)** [83].

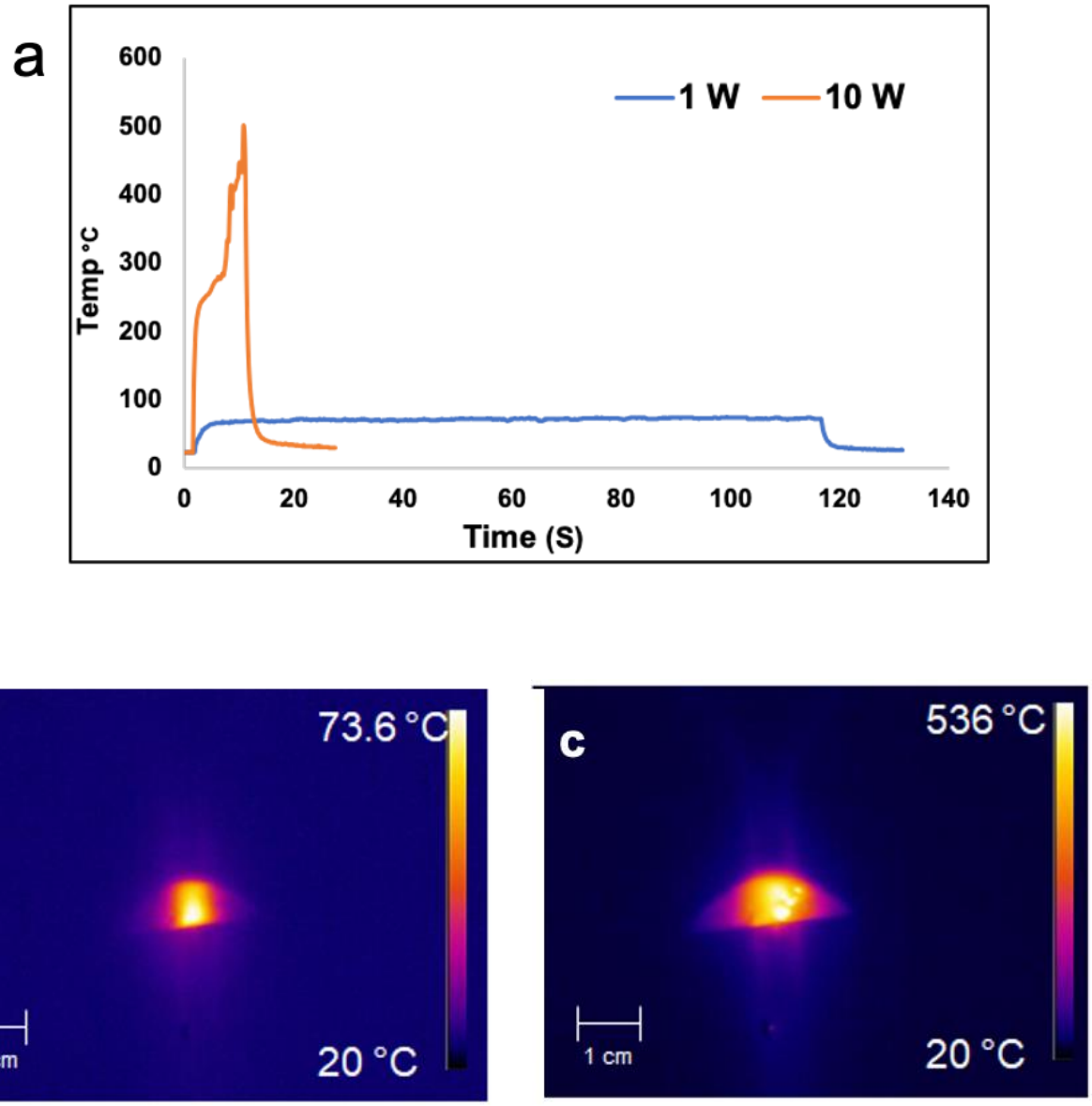

Figure 10. a) Radio Frequency (RF) response of $Ti_3C_2T_z$ at 1 W (135 MHz) and 10 W (135 MHz) power; b) Thermal Images of RF response of $Ti_3C_2T_z$ at 1 W (135 MHz) and; c)10 W (135 MHz) power.

4.3 Supercapacitor Electrode

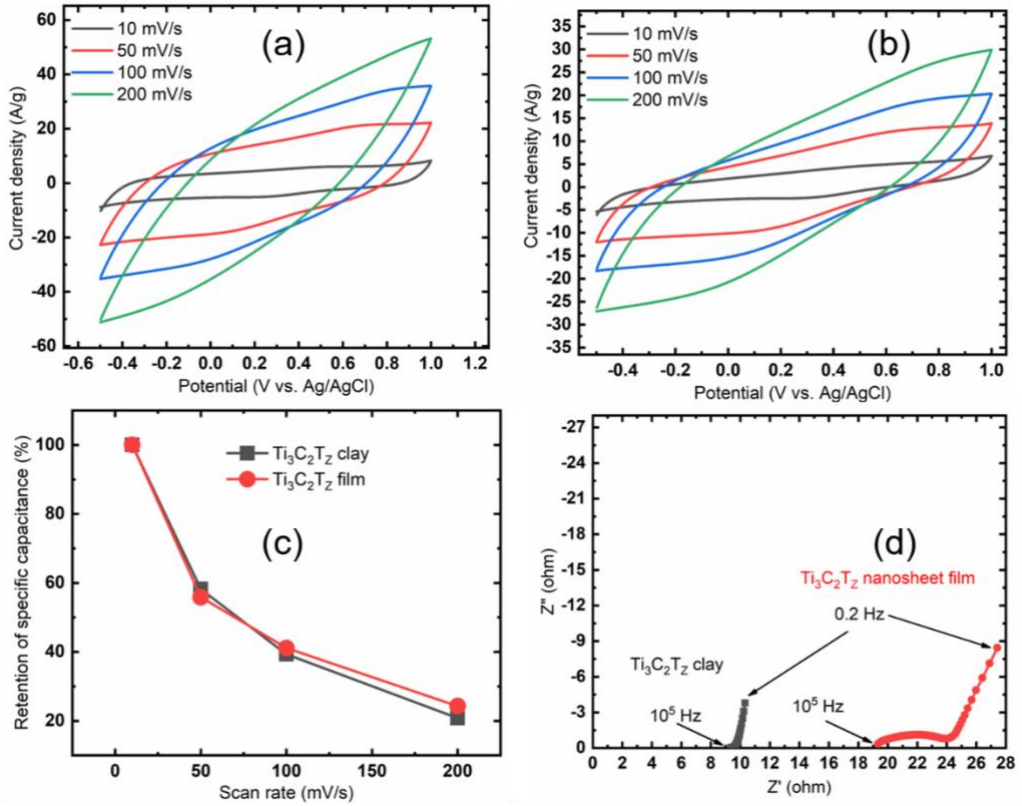

Figure 11. Current density vs. potential (CV) curves for (a) $Ti_3C_2T_z$ clay and (b) $Ti_3C_2T_z$ film; (c) Capacitance retention of $Ti_3C_2T_z$ clay and $Ti_3C_2T_z$ film with increasing scan rate; (d) Nyquist plots of $Ti_3C_2T_z$ clay and $Ti_3C_2T_z$ film.

Figure 11a & 11b shows the three-electrode CV curves of $Ti_3C_2T_z$ clay and $Ti_3C_2T_z$ nanosheet film at different scan rates in 1 M H_2SO_4 electrolyte. $Ti_3C_2T_z$ clay and nano-sheets (deposited on carbon paper) were used as the working electrode, while a platinum wire and Ag/AgCl were used as counter and reference electrodes, respectively. Both CVs show almost EDLC nature with a small feature at ~0.8 V. However, the current response of $Ti_3C_2T_z$ clay is significantly higher than that of $Ti_3C_2T_z$ film. Both CV curves show a wide potential window of -0.5 V to 1 V. Both CV plots are undistorted even at a high scan rate of 200 mV/s. The specific capacitance of $Ti_3C_2T_z$ clay and $Ti_3C_2T_z$ film were measured using the three-electrode method at various scan rates

presented in **Table 3**. Both $Ti_3C_2T_z$ clay and $Ti_3C_2T_z$ film showed maximum specific capacitances of 519 and 428 F/g at a 10 mV/s scan rate. Comparison of the specific capacitance obtained in this work with previously published results for $Ti_3C_2T_z$ obtained using conventional etching techniques (**Table 4**) clearly show enhanced performance (by 99%) of $Ti_3C_2T_z$ etched in molten SnF_2 from 215 F/g to 428 F/g[84].

Scan rate (mV/s)	**Specific capacitance (F/g)**	
	$Ti_3C_2T_z$ clay	**$Ti_3C_2T_z$ nanosheets**
10	519	428
50	302	239
100	204	176
200	108	104

Table 3. The specific capacitance of $Ti_3C_2T_z$ clay and $Ti_3C_2T_z$ film were measured using the three-electrode method at various scan rates.

	Specific Capacitance (F/g)	**Scan Rate**	**Reference**
$Ti_3C_2T_X$ Nanosheets	215	10 mV/s	[84]
$Ti_3C_2T_X$ clay	246	2 mV/s	[22]
$Ti_3C_2T_X$	67.7	1 A /g	[52]
Intercalated with K^+ and calcinated $Ti_3C_2T_X$	500	1 mV/s	[85]
Surface-modified 2D titanium carbide	325	2 mV/s	[86]
$Ti_3C_2T_x$ hydrogel film	380	2 mV/s	[3]
Molten Salt Etched $Ti_3C_2T_z$	**428**	**10 mV/s**	**Present Work**

Table 4. Comparison of the specific capacitance (three electrode) of $Ti_3C_2T_z$ electrode with the present work.

Although the capacitance value of the $Ti_3C_2T_z$ clay was comparatively high, the retention value of $Ti_3C_2T_z$ film was slightly higher **(Figure 11c).** At 100 mV/s scan rate, the retention of $Ti_3C_2T_z$ clay and $Ti_3C_2T_z$ nanosheet or film was measured as 39 and 41%, respectively. On the other hand,

at 200 mV/s scan rate the retention value was 21 and 24% for $Ti_3C_2T_z$ clay and $Ti_3C_2T_z$ film, respectively. **Figure 11d** represents the Nyquist plot of EIS (electrochemical impedance spectroscopy) data of $Ti_3C_2T_z$ clay and $Ti_3C_2T_z$ film. The specific capacitance depends on the resistance formed at the electrode-electrolyte interface (series resistance) and the active material's charge transfer resistance (Faradic resistance). The series resistance of $Ti_3C_2T_z$ nanosheets or film was comparatively higher (~19.2 ohm) than that of $Ti_3C_2T_z$ clay (~9.2 ohm) corresponding equivalent circuit is showed in **Figure 12**. The agglomeration of the nanosheets may be the reason for lower conductivity and high series resistance of $Ti_3C_2T_z$ films. Faradaic resistance of $Ti_3C_2T_z$ clay was very low ~ 0.2 ohm. Due to the low Faradic resistance, $Ti_3C_2T_z$ clay exhibited high specific capacitance. The Faradic resistance of $Ti_3C_2T_z$ nanosheets film was 2.5 ohm.

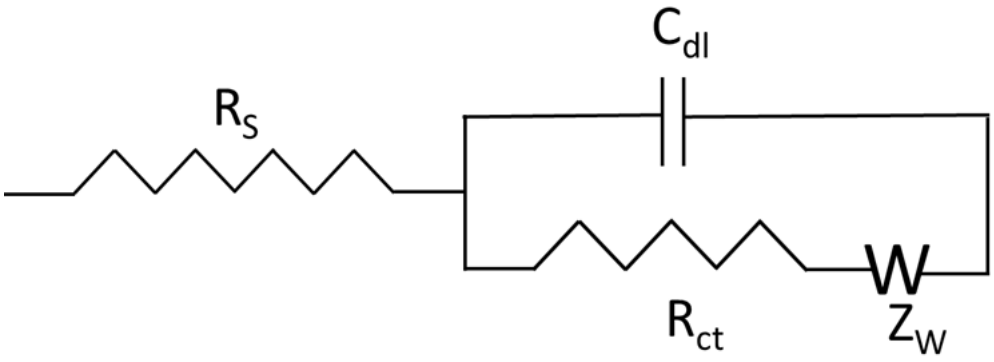

Figure 12. Equivalent circuit: Rs is the series resistance, C_{dl} is the capacitance, R_{ct} is the faradic or charge transfer resistance and Zw is the Warburg element.

Figure 13a and 13b represents the two electrode CV of $Ti_3C_2T_z$ clay and $Ti_3C_2T_z$ film within a potential window of 0 to 1 V. The CV shows EDLC nature and sustained its nature at a very high scan rate of 200 mV/s. The specific capacitance was calculated from the CV as 43 and 33 mF/cm^2 for $Ti_3C_2T_z$ clay and $Ti_3C_2T_z$ film, respectively. **Figure 13c** represents the charge-discharge profile of $Ti_3C_2T_z$ clay and $Ti_3C_2T_z$ film at a constant current density of 1 mA/cm^2. The specific

capacitance of $Ti_3C_2T_z$ clay and $Ti_3C_2T_z$ nanosheets was also calculated from the CD curve as 56 and 52 mF/cm^2, respectively. The power and energy density were also calculated from the CD. The energy density of $Ti_3C_2T_z$ clay and $Ti_3C_2T_z$ nanosheets film was calculated as 7.8 and 7.2 μW h/cm^2 at a power density of 500 μW/cm^2. Comparison of present work with published data **(Table 5)** shows the considerable improvement of results and also, we can see the little bit of tradeoff between energy and power density values.

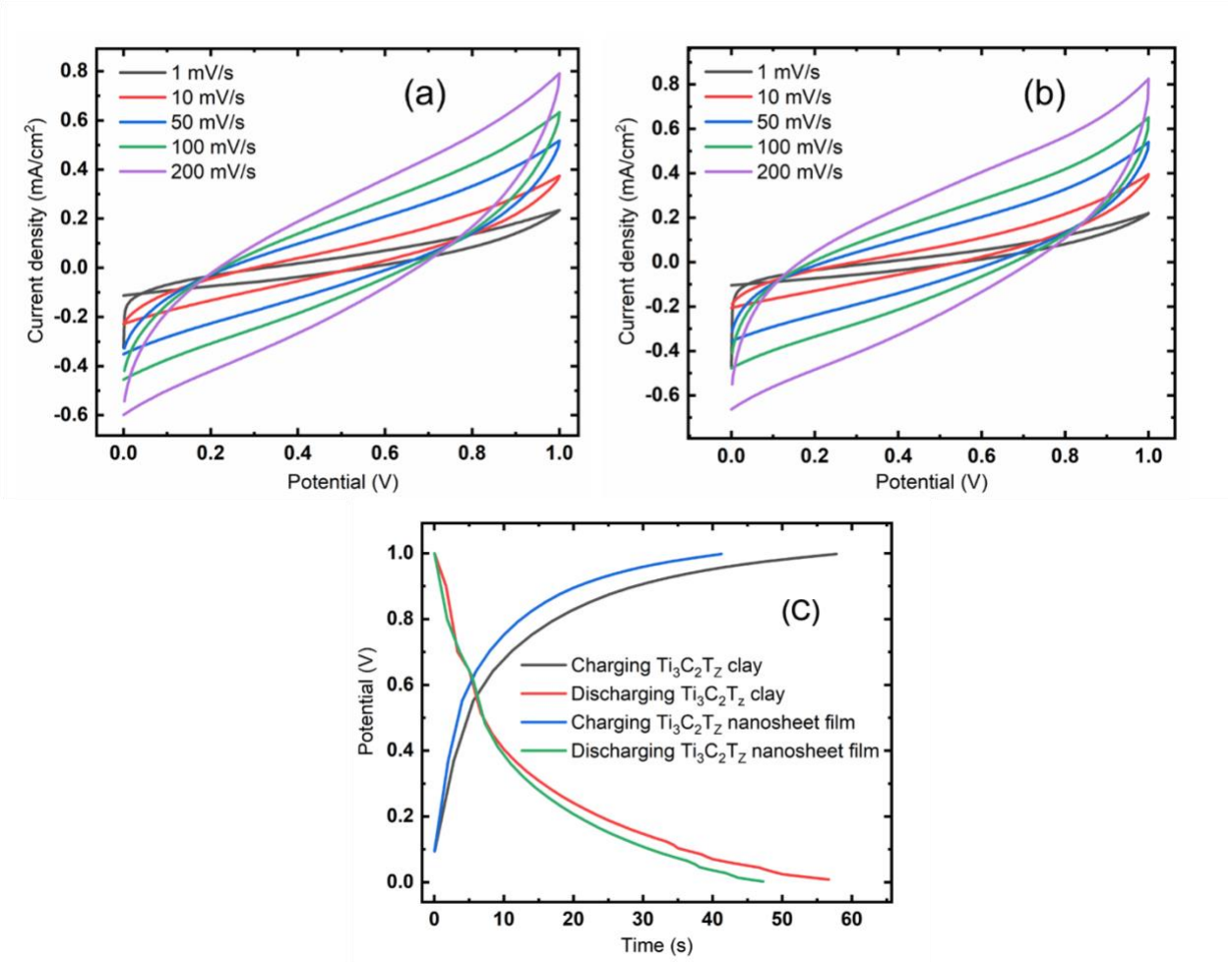

Figure 13. Two electrode CV of (a) $Ti_3C_2T_z$ clay and (b) $Ti_3C_2T_z$ film at various scan rate; (c) Two electrode CD of (a) $Ti_3C_2T_z$ clay and (b) $Ti_3C_2T_z$ film at 1 mA/cm^2 current density.

	Energy density (μW h/cm^2)	**Corresponding Power density (μW/cm^2)**	**References**
3D MXene	24.4	640	[87]
3D MXene–Graphene Aerogel	2.18	60	[88]
Co-Al-LDH/MXene	8.84	230	[89]
Carbon//MXene	2.62	1620	[90]
3D Printed vanadium nitride (VN) nanowire/CNT	96	270	[91]
Additive-free MXene	0.32	11.4	[92]
Molten salt etched $Ti_3C_2T_z$	**7.8**	**500**	**Present Work**

Table 5. Comparison of the specific capacitance, energy density, power density (two electrode) of published data with the present work.

CHAPTER V CONCLUSION AND FUTURE SCOPE

5 Summary of Work

5.1 Conclusion

In conclusion, an alternative approach of molten salt etching is proposed as an alternative to the traditional HF etching. The new approach resulted in successful synthesis of water dispersible $Ti_3C_2T_z$. This new approach will open up the new avenues for safer scaled of $Ti_3C_2T_z$ production on a commercial level without the use of hazardous HF, or other acids. The SEM, TEM, EDS, and XRD confirm the formation of $Ti_3C_2T_z$ nanosheets by etching in the molten SnF_2 salt. However, the separation process is crucial to separate the $Ti_3C_2T_z$ nanosheets from the mixture of MAX phase spheres. The $Ti_3C_2T_z$ was used to make electrodes with a specific capacitance of 428 F/g (10 mV/s). These exciting findings open up a new, safe, industrially viable method to make dispersible $Ti_3C_2T_z$ nanosheets.

5.2 Future Scope

The current findings which we have reported so far are performed for $Ti_3C_2T_z$ MXene only. Currently, the method used (HF or *In-situ* HF) for the etching of V_2CT_z and Nb_2CT_z MXene results in the formation MXenes which are prone to oxidation and low yield of production. The MXene etched by molten salt etching contains halide terminated MXene and that might provide enhanced oxidation stability to MXene. Therefore, in future, we would like to expand our molten salt etching method for the development of other non-titanium MXene like V_2CT_z and Nb_2CT_z MXene. We have performed few preliminary experiments toward our goal of developing of non-titanium MXene and the results are presented below.

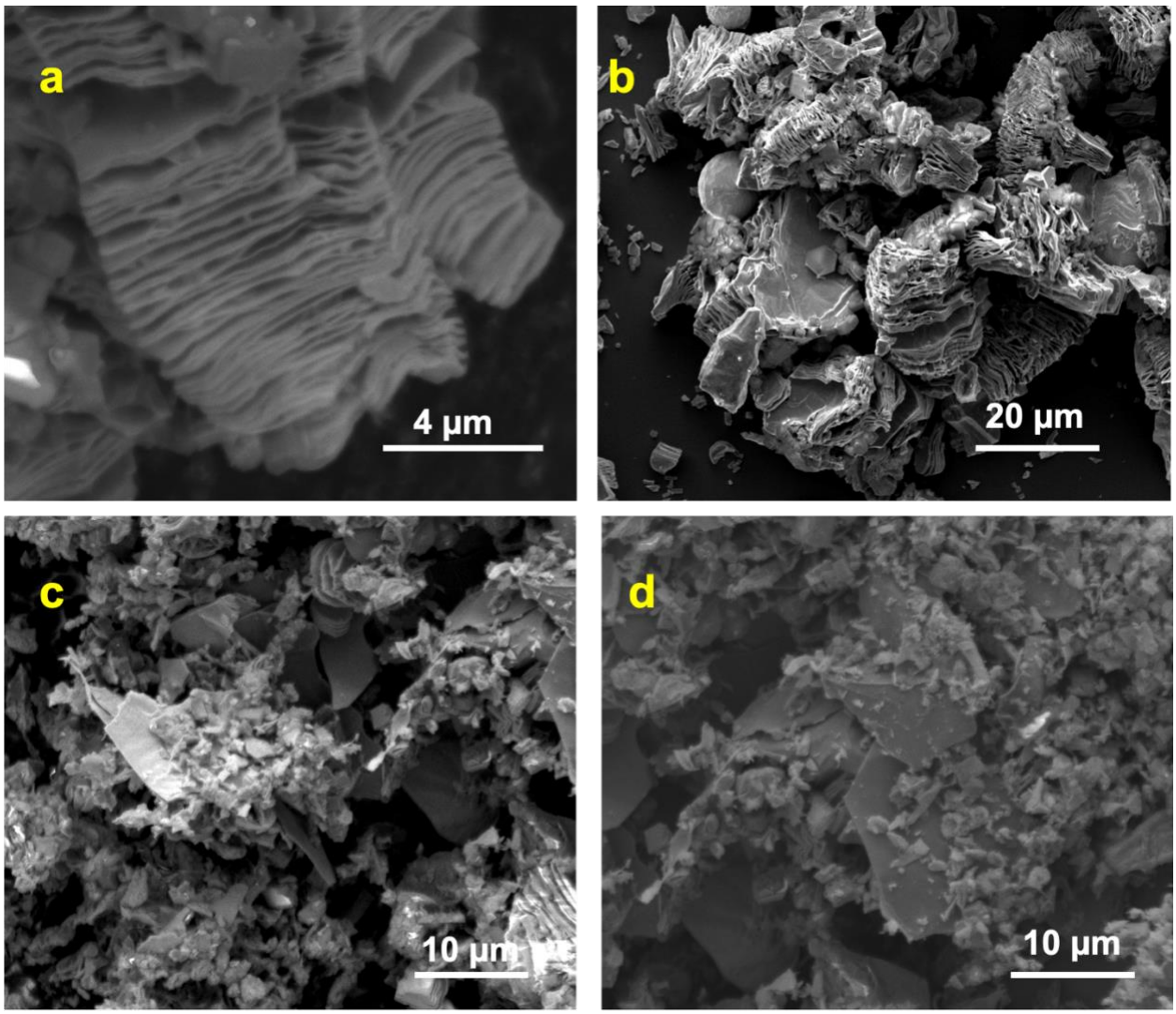

Figure 14. SEM Image of: (a) Nb_2CT_z before KOH wash (freeze dried); (b) Nb_2CT_z after KOH wash (freeze dried); (c) and(d) Nb_2CT_z nanosheets.

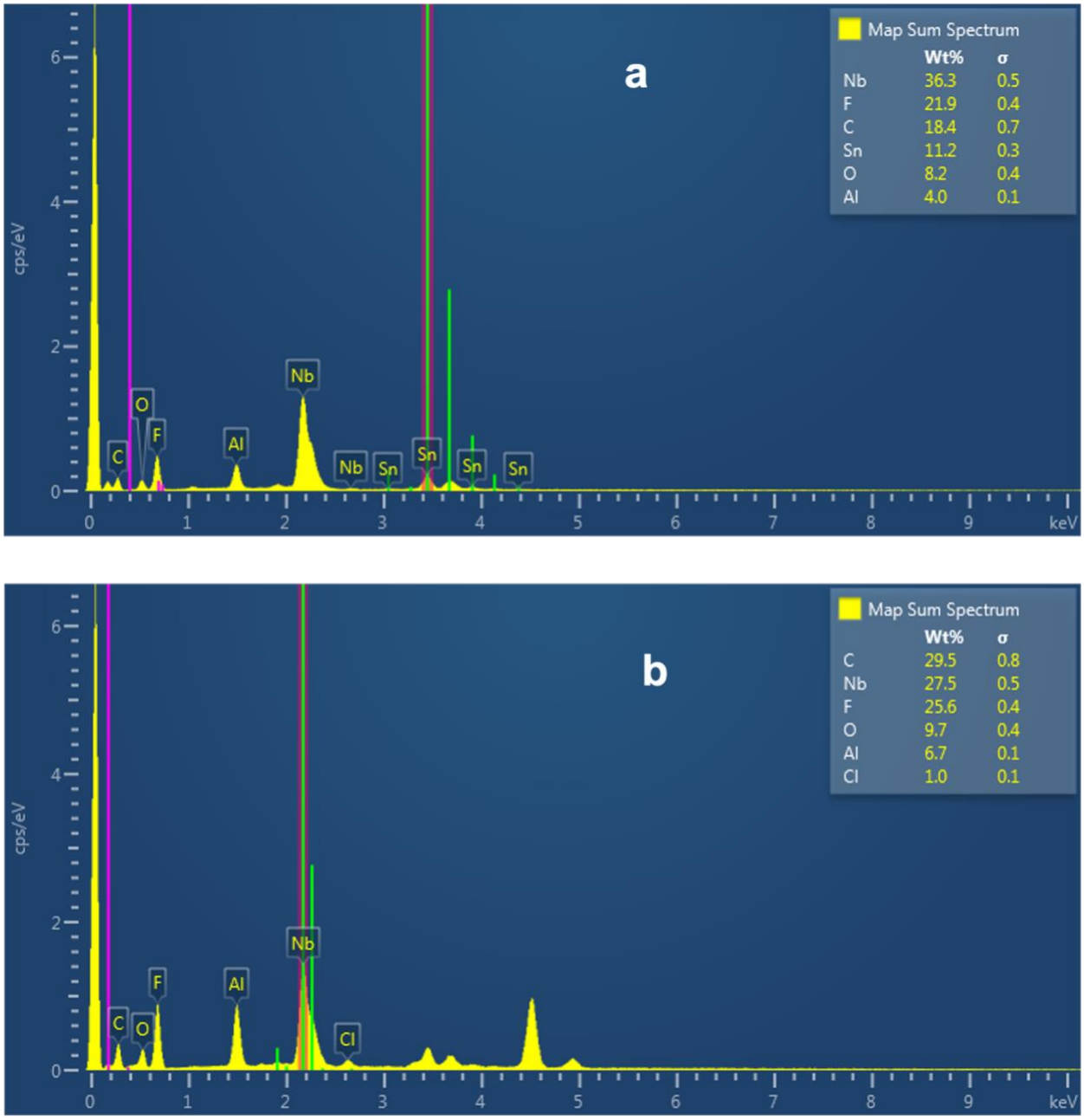

Figure 15. EDS of Nb_2CT_z clay and nanosheets Nb_2CT_z (supernatant).

Figure 14a and 14b, SEM clearly shows the accordion-like structure of clay, which is an indication of an etching of A layer from the parent MAX phase. EDS showed in **Figure 15** confirms the etching of MAX phase to MXene. The 4 wt.% of Al clearly indicates that Al has been etched out of the MAX phase to form Nb_2CT_z. The presence of 11. 2 wt. % of Sn in EDS is the

result of the formation of Sn (a byproduct of etching reaction). The **Figure 13c and 13d** show the presence of few Nb_2CT_z nanosheets along with other small material. The goal of the next experiment will be the separation of nanosheets from that small stuff. The formed dispersion of Nb_2CT_z found to be colloidally stable for a week (visual observations).

This method avoids the usage of HF for the production of MXene which makes it more suitable for the production of MXene at a large scale without much danger of HF.

REFERENCES

1. Naguib, M., et al., *Two-dimensional nanocrystals produced by exfoliation of Ti3AlC2.* Advanced materials, 2011. **23**(37): p. 4248-4253.
2. Naguib, M., et al., *Two-dimensional transition metal carbides.* ACS nano, 2012. **6**(2): p. 1322-1331.
3. Lukatskaya, M.R., et al., *Ultra-high-rate pseudocapacitive energy storage in two-dimensional transition metal carbides.* Nature Energy, 2017. **2**(8): p. 1-6.
4. Brownson, D.A.C., D.K. Kampouris, and C.E. Banks, *An Overview of Graphene in Energy Production and Storage Applications.* J. Power Sources, 2011. **196**: p. 4873.
5. Shirshova, N., et al., *Multifunctional structural energy storage composite supercapacitors.* Faraday discussions, 2014. **172**: p. 81-103.
6. Tang, Q., Z. Zhou, and P. Shen, *Are MXenes promising anode materials for Li ion batteries? Computational studies on electronic properties and Li storage capability of Ti3C2 and Ti3C2X2 (X= F, OH) monolayer.* Journal of the American Chemical Society, 2012. **134**(40): p. 16909-16916.
7. Anasori, B., M.R. Lukatskaya, and Y. Gogotsi, *2D metal carbides and nitrides (MXenes) for energy storage.* Nature Reviews Materials, 2017. **2**(2): p. 1-17.
8. Li, L., et al., *Smart MXene-Based Janus Films with Multi-responsive Actuation Capability and High Electromagnetic Interference Shielding Performances.* Carbon, 2020.
9. Shahzad, F., et al., *Electromagnetic interference shielding with 2D transition metal carbides (MXenes).* Science, 2016. **353**(6304): p. 1137-1140.

10. Seh, Z.W., et al., *Two-dimensional molybdenum carbide (MXene) as an efficient electrocatalyst for hydrogen evolution.* ACS Energy Letters, 2016. **1**(3): p. 589-594.

11. Ran, J., et al., *Ti_3C_2 MXene co-catalyst on metal sulfide photo-absorbers for enhanced visible-light photocatalytic hydrogen production.* 2017.

12. Naguib, M., et al., *25th anniversary article: MXenes: a new family of two-dimensional materials.* Advanced materials, 2014. **26**(7): p. 992-1005.

13. Lakhe, P., et al., *Process Safety Analysis for Ti3C2T x MXene Synthesis and Processing.* Industrial & Engineering Chemistry Research, 2019. **58**(4): p. 1570-1579.

14. Sun, W., et al., *Electrochemical etching of Ti 2 AlC to Ti 2 CT x (MXene) in low-concentration hydrochloric acid solution.* Journal of Materials Chemistry A, 2017. **5**(41): p. 21663-21668.

15. Urbankowski, P., et al., *Synthesis of two-dimensional titanium nitride Ti 4 N 3 (MXene).* Nanoscale, 2016. **8**(22): p. 11385-11391.

16. Barsoum, M.W., *The MN+ 1AXN phases: A new class of solids: Thermodynamically stable nanolaminates.* Progress in solid state chemistry, 2000. **28**(1-4): p. 201-281.

17. Eklund, P., et al., *The Mn+ 1AXn phases: Materials science and thin-film processing.* Thin Solid Films, 2010. **518**(8): p. 1851-1878.

18. Eklund, P., J. Rosen, and P.O.Å. Persson, *Layered ternary M n+ 1AX n phases and their 2D derivative MXene: an overview from a thin-film perspective.* Journal of Physics D: Applied Physics, 2017. **50**(11): p. 113001.

19. Shah, S., et al., *Template-free 3D titanium carbide (Ti 3 C 2 T x) MXene particles crumpled by capillary forces.* Chemical Communications, 2017. **53**(2): p. 400-403.

20. Khazaei, M., et al., *Electronic properties and applications of MXenes: a theoretical review.* Journal of Materials Chemistry C, 2017. **5**(10): p. 2488-2503.

21. Li, M., et al., *Novel Scale-Like Structures of Graphite/TiC/Ti3C2 Hybrids for Electromagnetic Absorption.* Advanced Electronic Materials, 2018. **4**(5): p. 1700617.

22. Ghidiu, M., et al., *Conductive two-dimensional titanium carbide 'clay' with high volumetric capacitance.* Nature, 2014. **516**(7529): p. 78-81.

23. Persson, I., et al., *2D transition metal carbides (MXenes) for carbon capture.* Advanced Materials, 2019. **31**(2): p. 1805472.

24. Kim, S.J., et al., *Metallic Ti3C2T x MXene gas sensors with ultrahigh signal-to-noise ratio.* ACS nano, 2018. **12**(2): p. 986-993.

25. Ronchi, R.M., J.T. Arantes, and S.F. Santos, *Synthesis, structure, properties and applications of MXenes: Current status and perspectives.* Ceramics International, 2019. **45**(15): p. 18167-18188.

26. Feng, A., et al., *Fabrication and thermal stability of NH4HF2-etched Ti3C2 MXene.* Ceramics International, 2017. **43**(8): p. 6322-6328.

27. Li, T., et al., *Fluorine-free synthesis of high-purity Ti3C2Tx (T= OH, O) via alkali treatment.* Angewandte Chemie International Edition, 2018. **57**(21): p. 6115-6119.

28. Li, M., et al., *Element replacement approach by reaction with Lewis acidic molten salts to synthesize nanolaminated MAX phases and MXenes*. Journal of the American Chemical Society, 2019. **141**(11): p. 4730-4737.

29. Li, Y., et al., *A general Lewis acidic etching route for preparing MXenes with enhanced electrochemical performance in non-aqueous electrolyte.* Nature Materials, 2020: p. 1-6.

30. Kamysbayev, V., et al., *Covalent surface modifications and superconductivity of two-dimensional metal carbide MXenes.* Science, 2020. **369**(6506): p. 979-983.

31. Bai, Y., et al., *Dependence of elastic and optical properties on surface terminated groups in two-dimensional MXene monolayers: a first-principles study.* RSC advances, 2016. **6**(42): p. 35731-35739.

32. Zha, X.-H., et al., *Role of the surface effect on the structural, electronic and mechanical properties of the carbide MXenes.* EPL (Europhysics Letters), 2015. **111**(2): p. 26007.

33. Wang, K., et al., *Fabrication and thermal stability of two-dimensional carbide Ti3C2 nanosheets.* Ceramics International, 2016. **42**(7): p. 8419-8424.

34. Michael, J., Z. Qifeng, and W. Danling, *Titanium carbide MXene: Synthesis, electrical and optical properties and their applications in sensors and energy storage devices.* Nanomaterials and Nanotechnology, 2019. **9**: p. 1847980418824470.

35. Tang, X., et al., *2D metal carbides and nitrides (MXenes) as high-performance electrode materials for lithium-based batteries.* Advanced Energy Materials, 2018. **8**(33): p. 1801897.

36. Becerril, H.A., et al., *Evaluation of solution-processed reduced graphene oxide films as transparent conductors.* ACS nano, 2008. **2**(3): p. 463-470.

37. Dillon, A.D., et al., *Highly conductive optical quality solution-processed films of 2D titanium carbide.* Advanced Functional Materials, 2016. **26**(23): p. 4162-4168.

38. Bairi, P., et al., *Mesoporous graphitic carbon microtubes derived from fullerene C 70 tubes as a high performance electrode material for advanced supercapacitors.* Journal of Materials Chemistry A, 2016. **4**(36): p. 13899-13906.

39. Sood, P., K.C. Kim, and S.S. Jang, *Electrochemical and electronic properties of nitrogen doped fullerene and its derivatives for lithium-ion battery applications.* Journal of energy chemistry, 2018. **27**(2): p. 528-534.

40. Zhang, R., F. Mizuno, and C. Ling, *Fullerenes: non-transition metal clusters as rechargeable magnesium battery cathodes.* Chemical Communications, 2014. **51**(6): p. 1108-1111.

41. Balasingam, S.K., J.S. Lee, and Y. Jun, *Molybdenum diselenide/reduced graphene oxide based hybrid nanosheets for supercapacitor applications.* Dalton Transactions, 2016. **45**(23): p. 9646-9653.

42. Wang, X., et al., *Hybrid two-dimensional materials in rechargeable battery applications and their microscopic mechanisms.* Chemical Society Reviews, 2016. **45**(15): p. 4042-4073.

43. Sofer, Z., et al., *Few-layer black phosphorus nanoparticles.* Chemical communications, 2016. **52**(8): p. 1563-1566.

44. Xia, Q., et al., *Phosphorus and phosphide nanomaterials for sodium-ion batteries.* Nano Research, 2017. **10**(12): p. 4055-4081.

45. Zou, X., et al., *Energy storage properties of selectively functionalized Cr-group MXenes.* Computational Materials Science, 2018. **150**: p. 236-243.

46. Nan, J., et al., *Nanoengineering of 2D MXene-based materials for energy storage applications.* Small, 2019: p. 1902085.

47. Cai, M., et al., *Fast response, vertically oriented graphene nanosheet electric double layer capacitors synthesized from C2H2.* Acs Nano, 2014. **8**(6): p. 5873-5882.

48. Wu, Z.-S., et al., *High-energy MnO2 nanowire/graphene and graphene asymmetric electrochemical capacitors.* ACS nano, 2010. **4**(10): p. 5835-5842.

49. Lan, D., et al., *Mesoporous CoO nanocubes@ continuous 3D porous carbon skeleton of rose-based electrode for high-performance supercapacitor.* ACS applied materials & interfaces, 2014. **6**(15): p. 11839-11845.

50. Stoller, M.D. and R.S. Ruoff, *Best Practice Methods for Determining an Electrode Material's Performance for Ultracapacitors.* Energy Environ. Sci., 2010. **3**: p. 1294.

51. Carlson, T. and L. Asp. *Carbon fibre composites capacitors for short term electric energy storage in structural applications*. in *International Conference on Composites Materials: 21/08/2011-26/08/2011*. 2011.

52. Zang, X., et al., *Enhancing capacitance performance of Ti 3 C 2 T x MXene as electrode materials of supercapacitor: from controlled preparation to composite structure construction.* Nano-Micro Letters, 2020. **12**(1): p. 1-24.

53. Stoller, M.D., et al., *Graphene-Based Ultracapacitors.* Nano Lett., 2008. **8**: p. 3498.

54. Weng, Z., et al., *Graphene–Cellulose Paper Flexible Supercapacitors.* Adv. Energy Mater., 2011. **1**: p. 917.

55. Sumboja, A., et al., *Large Areal Mass, Flexible and Free-Standing Reduced Graphene Oxide/Manganese Dioxide Paper for Asymmetric Supercapacitor Device.* Adv. Mater., 2013. **25**: p. 2809.

56. Wang, Y., et al., *Supercapacitor devices based on graphene materials.* The Journal of Physical Chemistry C, 2009. **113**(30): p. 13103-13107.

57. Byon, H.R., et al., *Thin films of carbon nanotubes and chemically reduced graphenes for electrochemical micro-capacitors.* Carbon, 2011. **49**(2): p. 457-467.

58. Maiti, U.N., et al., *Three-dimensional shape engineered, interfacial gelation of reduced graphene oxide for high rate, large capacity supercapacitors.* Advanced materials, 2014. **26**(4): p. 615-619.

59. Lukatskaya, M.R., et al., *Cation intercalation and high volumetric capacitance of two-dimensional titanium carbide.* Science, 2013. **341**(6153): p. 1502-1505.

60. Ghidiu, M., et al., *Synthesis and characterization of two-dimensional Nb 4 C 3 (MXene).* Chemical communications, 2014. **50**(67): p. 9517-9520.

61. Rao, D., et al., *Mechanism on the improved performance of lithium sulfur batteries with MXene-based additives.* The Journal of Physical Chemistry C, 2017. **121**(21): p. 11047-11054.

62. Jeon, N.J., et al., *Compositional engineering of perovskite materials for high-performance solar cells.* Nature, 2015. **517**(7535): p. 476-480.

63. Lo, S.-C., et al. *Design and implementation of a novel poly-Si single proof-mass differential capacitive-sensing 3-axis accelerometer*. in *2013 Transducers & Eurosensors XXVII: The 17th International Conference on Solid-State Sensors, Actuators and Microsystems (TRANSDUCERS & EUROSENSORS XXVII)*. 2013. IEEE.

64. Pang, D., et al., *Electrochemical Actuators Based on Two-Dimensional Ti3C2T x (MXene).* Nano letters, 2019. **19**(10): p. 7443-7448.

65. Zhang, W.-M., et al., *Electrostatic pull-in instability in MEMS/NEMS: A review.* Sensors and Actuators A: Physical, 2014. **214**: p. 187-218.

66. Tabassian, R., et al., *Functionally Antagonistic Hybrid Electrode with Hollow Tubular Graphene Mesh and Nitrogen-Doped Crumpled Graphene for High-Performance Ionic Soft Actuators.* Advanced Functional Materials, 2018. **28**(5): p. 1705714.

67. Mukai, K., et al., *Highly conductive sheets from millimeter-long single-walled carbon nanotubes and ionic liquids: application to fast-moving, low-voltage electromechanical actuators operable in air.* Advanced materials, 2009. **21**(16): p. 1582-1585.

68. Dai, M., et al., *Humidity-responsive bilayer actuators based on a liquid-crystalline polymer network.* ACS applied materials & interfaces, 2013. **5**(11): p. 4945-4950.

69. Cai, G., et al., *Leaf-inspired multiresponsive MXene-based actuator for programmable smart devices.* Science advances, 2019. **5**(7): p. eaaw7956.

70. Nguyen, V.H., et al., *Stimuli-Responsive MXene-Based Actuators.* Advanced Functional Materials, 2020: p. 1909504.

71. Zavahir, S., et al., *Ti3C2Tx MXene-Based Light-Responsive Hydrogel Composite for Bendable Bilayer Photoactuator.* Nanomaterials, 2020. **10**(7): p. 1419.

72. Hantanasirisakul, K. and Y. Gogotsi, *Electronic and optical properties of 2D transition metal carbides and nitrides (MXenes).* Advanced materials, 2018. **30**(52): p. 1804779.

73. Cao, W.-T., et al., *Two-dimensional MXene-reinforced robust surface superhydrophobicity with self-cleaning and photothermal-actuating binary effects.* Materials Horizons, 2019. **6**(5): p. 1057-1065.

74. Ling, Z., et al., *Flexible and conductive MXene films and nanocomposites with high capacitance.* Proceedings of the National Academy of Sciences, 2014. **111**(47): p. 16676-16681.

75. Naguib, M., et al., *Ti 3 C 2 T x (MXene)–polyacrylamide nanocomposite films.* RSC Advances, 2016. **6**(76): p. 72069-72073.

76. Chen, J., et al., *CO 2 and temperature dual responsive "Smart" MXene phases.* Chemical Communications, 2015. **51**(2): p. 314-317.

77. Sobolčiak, P., et al., *2D Ti3C2Tx (MXene)-reinforced polyvinyl alcohol (PVA) nanofibers with enhanced mechanical and electrical properties.* PLoS One, 2017. **12**(8): p. e0183705.

78. Zhi, W., et al., *Study of MXene-filled polyurethane nanocomposites prepared via an emulsion method.* Composites Science and Technology, 2018. **168**: p. 404-411.

79. Huang, Z., et al., *Structure and crystallization behavior of poly (ethylene oxide)/Ti3C2Tx MXene nanocomposites.* Polymer, 2016. **102**: p. 119-126.

80. Zhang, H., et al., *Preparation, mechanical and anti-friction performance of MXene/polymer composites.* Materials & Design, 2016. **92**: p. 682-689.

81. Iqbal, M.A., et al., *Ti3C2-MXene/Bismuth ferrite nanohybrids for efficient degradation of organic dyes and colorless pollutants.* ACS omega, 2019. **4**(24): p. 20530-20539.

82. Li, M., et al., *Element Replacement Approach by Reaction with Lewis Acidic Molten Salts to Synthesize Nanolaminated MAX Phases and MXenes.* Journal of the American Chemical Society, 2019. **141**(11): p. 4730-4737.

83. Habib, T., et al., *Heating of Ti 3 C 2 T x MXene/polymer composites in response to Radio Frequency fields.* Scientific reports, 2019. **9**(1): p. 1-7.

84. Zhang, X., et al., *Surface modified MXene film as flexible electrode with ultrahigh volumetric capacitance.* Electrochimica Acta, 2019. **294**: p. 233-239.

85. Li, J., et al., *Achieving high pseudocapacitance of 2D titanium carbide (MXene) by cation intercalation and surface modification.* Advanced Energy Materials, 2017. **7**(15): p. 1602725.

86. Dall'Agnese, Y., et al., *High capacitance of surface-modified 2D titanium carbide in acidic electrolyte.* Electrochemistry Communications, 2014. **48**: p. 118-122.

87. Yang, W., et al., *3D printing of freestanding MXene architectures for current-collector-free supercapacitors.* Advanced materials, 2019. **31**(37): p. 1902725.

88. Yue, Y., et al., *Highly self-healable 3D microsupercapacitor with MXene–graphene composite aerogel.* Acs Nano, 2018. **12**(5): p. 4224-4232.

89. Xu, S., et al., *Screen-printable microscale hybrid device based on MXene and layered double hydroxide electrodes for powering force sensors.* Nano energy, 2018. **50**: p. 479-488.

90. Wang, N., et al., *Laser-cutting fabrication of MXene-based flexible micro-supercapacitors with high areal capacitance.* ChemNanoMat, 2019. **5**(5): p. 658-665.

91. Zhang, Q., et al., *Wrapping aligned carbon nanotube composite sheets around vanadium nitride nanowire arrays for asymmetric coaxial fiber-shaped supercapacitors with ultrahigh energy density.* Nano letters, 2017. **17**(4): p. 2719-2726.

92. Zhang, C.J., et al., *Additive-free MXene inks and direct printing of micro-supercapacitors.* Nature communications, 2019. **10**(1): p. 1-9.